An experimental Study on the Motion and Fixed Points of a Light Sphere in a Stokes' Flow

A thesis submitted to the University of Manchester for the degree of

Doctor of Philosophy

in the Faculty of Engineering and Physical Sciences

2016

Tania Sauma Pérez

School of Physics and Astronomy

Contents

Word count: 14560

List of Tables

List of Figures

Abstract

An Experimental study on the dynamics of a positively buoyant sphere immersed in a rotating viscous flow is presented. For a smooth solid sphere it was found that the it sits at the centre of the cylinder for high Reynolds number Re. When decreasing Re the sphere settles at an eccentric equilibrium position, which existence cannot be explained by Stokesian calculations. The position of the fixed points is well predicted by a model that assumes small but finite Re. If Re is further decreased beyond a critical value Re_c, the sphere starts oscillating about the original fixed point, describing periodic circular orbits. For very small values of the Reynolds number the sphere settles at a fixed point by the wall of the cylinder, which becomes unstable to vertical oscillations. A exhaustive study of this dynamic is presented.

For a porous sphere it was found that the aforementioned eccentric fixed point exist, but in comparison with the solid case, remained much closer to the central axis of the cylinder. It was found that the stability range of this fixed point was larger than for the solid case.

Three spheres of different roughness were also studied, no significant effect on the eccentric fixed point or in the onset of the instability was found, showing that the fixed point is robust.

Declaration

No portion of the work referred to in this thesis has been submitted in support of an application for another degree or qualification of this or any other university or other institution of learning.

Acknowledgments

I have had a lot of crazy ideas in my life, but taking that plane across the Atlantic to come to Manchester, inspired by the romantic idea that Reynolds was here once too, without thinking that living so close to the north pole could be difficult for a creature of the desert like me, has been the craziest. I would like to thank some people that helped me to deal with this mayhem and to get a PhD in the process.

I have no words to say how honoured I am for being the last student of Professor Tom Mullin. Thank you for your guidance through this process, and for believing in me even before we met just because I showed you some pretty pictures of hydrodynamic solitons. I also want to thank to Dr. Finn Box, I don't know what I'm more grateful for, if for reading this thesis or for taking care of me when I broke my foot or for making me buy a winter coat so I'd stop complaining about the weather. I would also like to thank to Dr. Chris Johnson for his interest in my experimental results and for coming up with a theoretical model that helped us to finish the story.

I would like to thank to Dr. Draga Philer-Puzovic for being so welcoming and for baking a cake for my birthday so I wouldn't have to. You taught me that to be a women in science is to be awesome. Also thanks to Dr. Anne Juel. To Lucie Ducloue, Pallav Kant, Edgard Häner and Andrés Franco for

creating such an amazing work environment where people can become friends instead or just colleges.

I'm also indebted to Prof. Nicolás Mujica and Prof. Marcel Clerc for guiding my first steps in experimental physics, now more than ever I'm truly convinced that what you are doing in Chile is world class science. I want to thank to Becas Chile for funding this PhD. and to the OMP their support through the entire PhD process.

Quiero agradecer a toda familia en español, por la fe absurda que tienen en mí, especialmente a mi mami por su paciencia, a mi papi por hacerme una lámpara de solcito, a mis guatacas por ser tan grandes y a la Samy por ser eterna. A mis abuelos, tíos y primos que me hacen el aguante a la distancia, yo siento su amor acá, en el polo doliente.

I would like to thank to my friends in spanglish, for being my famila away from home: a los sudakas de la mancunia, a Anilena y Rocío for the good times in Hulme and the potodancing, y a San Jiulm himself. A la Ange por ser mi mami y hacerme sopas y enseñarme que conectarse con el lado femenino del ser te fortalece. A la clika del 6-8 a.k.a conygham crew for the parking-lotting deluxe, al Tomy por preparar el café como si fuese un deber divino, al Mati por los viajes interestelares y al Sizor porque miau. To Tamara and Flo for helping me to be an entire person during the thesis writing, and because the house smelled like cake, instead of like misery, during the entire process. I'm also very grateful to all my compañeros, for showing me that everywhere in the world, there is people trying to create a better society.

Finalmente, al Ande, a la Pacha y al Inti. Me arden las alas de los zapatos por emprender el vuelo de regreso.

Copyright

Chapter 1

Introduction

The study of the dynamics of a sphere immersed in a rotating inviscid flow has been of the interest of scientists since the late XIX century with the seminal work of Sir William Thomson, titled "On the Ultramundane Corpuscles of Le Sage, also on the Motion of Rigid Solids in a Liquid circulating irrationally through perforations in them or in a Fixed Solid" [1].

In this work Sir Thomson states that "A properly trained dynamical intelligence would at once perceive that the constancy of moment of momentum round the axis, requires the globule to move directly towards it", or in other words; a solid sphere immersed in a rotating flow should remain at its axis of rotation.

Here we present the results of an experimental investigation into the motion of a positively buoyant particle immersed in a rotating viscous flow at low Reynolds number. As in the inviscid case the heavier fluid is thrown to the outside and the light sphere sits at an equilibrium position at the centre of the flow when Re is sufficiently high. Interestingly, there are also a set of eccentric stable fixed points at lower values of Re and these are found

to become unstable to simple oscillatory motion when Re is decreased.The dependance of the dynamics of the sphere on the size of the particle and the superficial roughness was investigated. The dynamics of a positively buoyant porous sphere was also studied.

The aims of this investigation were (a) to characterise the dynamics of a single positively buoyant sphere immersed in a rotating viscous flow at low Reynolds number, (b) to investigate the dependance of the different dynamical regimes to variations of size and roughness of the sphere, and (c) to inspire future theoretical work on the mentioned flow configuration by obtaining careful experimental data.

In section §1.1 the experimental parameters used through this investigation are discussed. The motivation for this experimental study is presented in section §1.2 with an emphasis on a direct application of this flow configuration, the bioreactor [2]. Previous experimental investigation concerning a particle immersed in a rotating flow are reviewed in section §1.3 . In section §1.4 a review on the state of the art of the theoretical literature about a particle free to move on a rotating viscous flow is presented. Finally, an outline of this thesis is presented in section §1.5.

1.1 Experimental Parameters

A diagram of the experimental parameters and their meaning is shown in figure 1.1.

The Reynolds number corresponds to the ratio between the inertial and the viscous forces in a fluid system. In the experimental realisations presented in this thesis two different Reynolds number are considered:

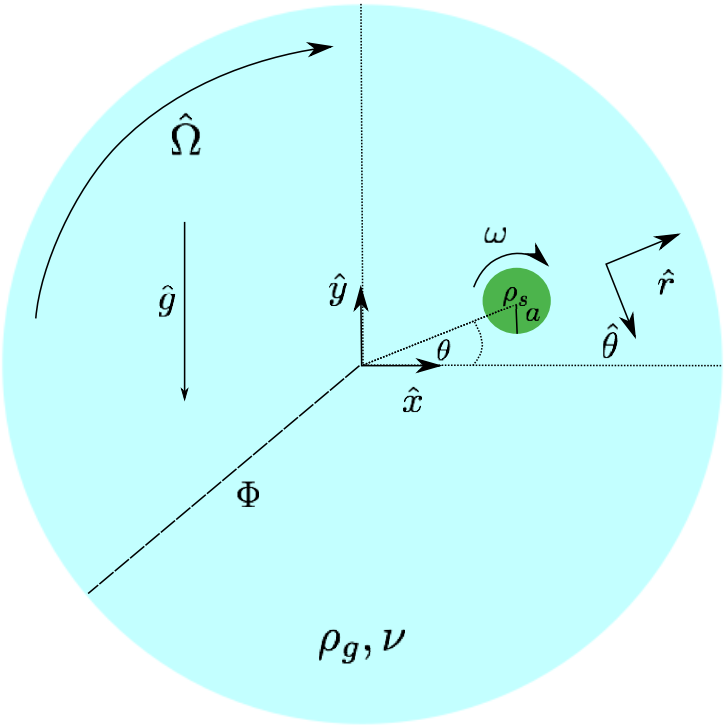

Figure 1.1: Schematics diagram of the experimental parameters considered in this thesis. Ω is the angular velocity of the rotating fluid, g is the acceleration of gravity, ρ_g is the density of the fluid, ν is the kinematic viscosity, a is the radius of the sphere, ρ_s is the density of the sphere, Φ is the radius of the cylinder and ω is the angular velocity of the sphere.

$$Re = \frac{a^2\Omega}{\nu}, \tag{1.1}$$

with a being the radius of the particle, Ω the angular velocity of the rotating drum and ν the kinematic viscosity of the fluid.

and

$$Re_p = \frac{aV_T}{\nu}, \tag{1.2}$$

where V_T corresponds to the terminal velocity of the sphere falling in an unbounded quiescent fluid.

The experiments presented in this document were performed at low Re, typically having a value between $0.01 < Re < 2$ which means that the viscous forces dominate the dynamics and the flow is considered to be Stokesian.

Another relevant parameter is the Stokes number, which correspond to the ratio between the relaxation time, the coefficient in the exponential decay of the speed of a settling object in a viscous fluid which is calculated as $t_0 = \frac{2}{9}a^2/\nu$, and the hydrodynamic time, given by the ratio between the size of the particle $2a$ and the speed of the fluid $a\Omega$. For a sphere in creeping flow is defined as

$$St = \frac{2a^2\Omega}{9\nu}, \tag{1.3}$$

which is proportional to the Reynolds number and had typical values between $0.01 < St < 0.25$.

The density ratio between the density of the sphere and the density of the fluid was defined as

$$P = \frac{\rho_s}{\rho_g} \tag{1.4}$$

and had typical values of $0.7 < P < 0.9$.

The other parameters correspond to the geometry of the system.

1.2 Motivation

The understanding of the dynamics of a single particle immersed in a rotating flow at low Reynolds number has both fundamental and practical importance.

Firstly, in the textbook of Guazelli and Morris [3] a study of the dynamics of a single particle is proposed as the simplest relevant case to achieve further understanding of a suspension of particles in a rotating flow. Secondly, suspension flows have many industrial applications, such as the manufacturing of precision latex microspheres through the use of a rotating latex reactor [4], [5] where this flow configuration is used to keep the particles on suspension without using more expensive devices to simulate microgravity, which is needed to avoid clustering of the seeded particles, fabricating monodisperse microspheres by keeping the particles steady during the polymerisation reaction. In the study by Roberts et al. [4] they use a a horizontally rotating cylinder, filled by a viscous fluid and place microspheres of about 3 micrometers. They found that the particles orbits in circles about a point displaced from the centre of the cylinder.

The motion of a sphere moving on a rotating flow at low Re is also relevant for the understanding of bioconvection [6], [7]. Bioconvection corresponds to the instability that a suspension of swimming algae or bacteria undergo due to differences in density distribution, if the organisms swim upwards and accumulate at a layer close to the surface, this region becomes denser. This unstable density distribution sets up a fluid motion analogous to that of a shallow fluid heated from the bottom.

A direct application of this flow configuration is the rotating bioreactor which is explained in detail in the next section.

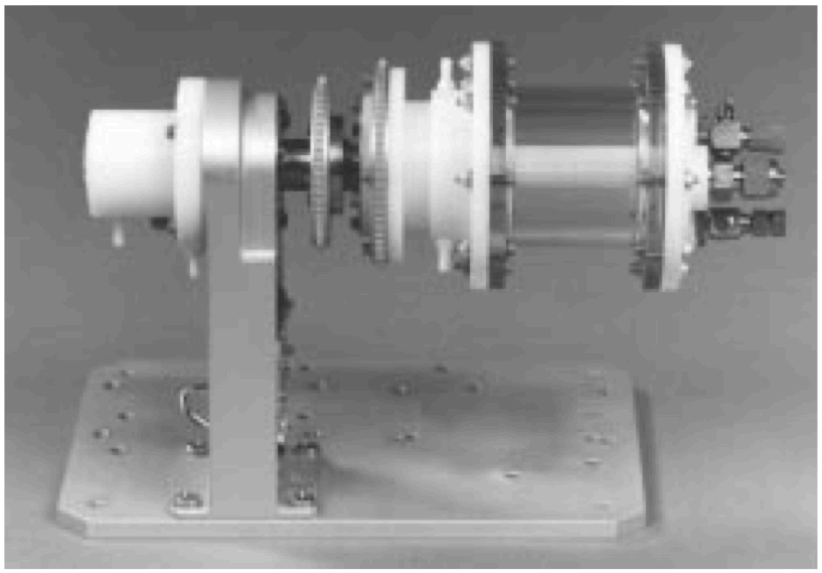

Figure 1.2: Bioreactor used by NASA for testing microgravity on earth. A biological scaffold, the microcarrier containing cells that will develop a tissue, is placed inside of the bioreactor. The cylinder is filled with water, and nutrients are infused into the fluid from the inner cylinder. The outer wall imposes a rotation to the fluid so the tissue inside of the scaffold can grow in a simulated microgravity environment

1.2.1 The rotating bioreactor

One of the main motivations to reach a better understanding of the dynamics of a sphere immersed in a rotating flow is the application of this flow configuration to tissue engineering.

Tissue engineering consists on creating functional tissue by using cells, scaffolds and biologically active molecules [8]. The aim is to restore or improve, from damaged tissue to entire organs. It can also be used to develop tissue for drug or chemical testing, among others applications.

Cultivating cells *in vitro*, in a static environment, make the cells to grow

in flat layers due to the effect of gravity acting constantly on the cells. This is different to what happens *in vivo*, inside of the body, where the cells grow three dimensionally [9]. A bioreactor is a device used in tissue engineering to grow organic tissue *in vitro* in a controlled environment develop by Schwarz and Wolf at NASA [2], [10] designed to neutralise this effect.

The bioreactor consist of a horizontally rotating vessel filled with fluid, typically water. This tissue culture technique allows tissue to be grown in a microgravity environment, because the tissue is in a state of constant free fall in the rotating fluid. Re has typical values of $0.8 < Re < 90$ and $0.17 < St < 20$ as calculated using the experimental parameters given by Dalwadi [11].

The specific type of bioreactor that resembles the flow configuration investigated in this thesis is the rotating wall vessel bioreactor, also know also as RWV [12]. The RWV bioreactor consists of two concentric cylinders, and the gap between them is completely filled with water that acts as culture media. The inner cylinder delivers nutrients and oxygen into the culture media while removing waste from it.

The cells that will develop to create the tissue of choice are seeded in a microcarrier that allows the exchange of nutrients with the surroundings. The scaffold, which is the construct formed by the microcarrier and the cells, is placed inside of the bioreactor. The external cylinder is rotated, and the entire fluid is in solid body rotation with the cylinder wall.

The selection of the density of the scaffold is of vital importance for the viability of the tissue; it has been observed by Gao et al. [13] and in other various studies [14], [15] and [16] that if the density of the scaffold is bigger than the density of the fluid ($P = 1.05$), the scaffold may collide with the

walls of the bioreactor, which could damage the tissue in the scaffold. In Gao's work it was also observed that if the density of the scaffold is smaller than the density of the fluid, the scaffold has an equilibrium position.

Some of the microcarriers used for tissue engineering are porous. This is to allow a better exchange of nutrients between the culture media and the tissue contained by the microcarrier. A complete review on the state of the art of mathematical modelling of tissue engineering focusing on porous scaffolds can be seen in the work of O'dea et al. [17] and in the work of Dalwadi [11].

An interesting experimental example is the study of Yu et al. [18], [19] on osteoblasts cultivated using a porous microcarrier inside of a high aspect ratio vessel rotating bioreactor. Scaffolds of different densities are fabricated by mixing heavier than water and lighter than water polymers. From their investigation is concluded that using the right kind of scaffold represents a great advantage against cultivating the tissue in a static environment in terms of phenotypic expression of the osteoblasts. This is because the nutrients penetrate better inside of the scaffold in a rotating bioreactor than in a static one, improving cell differentiation and mineralization.

Porous scaffolds are widely used in tissue engineering due to their mechanical properties [20]. Custom made designed scaffolds can guide cell growth and improve cell seeding and migration. For a review on porous scaffolds, read the work of Place et al. [21].

The selection of an scaffold of appropriate density is also stressed by Lappa [22]. In this work about a disk-like scaffold in a rotating wall perfused vessel is noted that choosing scaffolds and culture media of similar densities is needed to minimise shear and disturbances that might affect the development

of the tissue.

1.3 Experimental studies on a sphere in a rotating flow

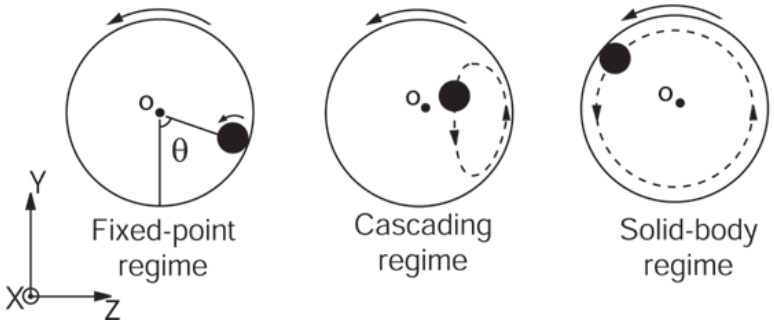

Figure 1.3: Different regimes for a heavy sphere in the work by Mullin et al. [23]. The Reynolds number increases from left to right showing the fixed point by the wall at the left, assymetrical oscillations at the middle and solid body motion at the right.

A wide variety of phenomena can be found when studying the dynamics of a particle inside a rotating drum filled with fluid. An experimental study conducted in a horizontal rotating cylinder filled with a viscous fluid by Mullin et al.[23], investigated the motion of a single heavy sphere and the interaction between two and three spheres. In their work, different dynamical regimes were identified for a single heavy sphere as the Reynolds number was increased from rest ($Re = 0$). The first described regime was a fixed point next to the wall described by the angle θ the sphere forms with the vertical. This angle θ increases with the Reynolds number until $\theta = 90°$, when the sphere detaches from the wall and starts oscillating, which is the second

regime described. This happens at Reynolds $Re > 1.21$. The square of the amplitude of these oscillations is linear with the Reynolds number, and the oscillation is periodic, which is consistent with a Hopf bifurcation.

Ashmore et al. [24] studied in detail the fixed point by the wall described above. When measuring the speed of rotation of the sphere, this differs from that of the wall such that the ratio between the speed of the sphere and the speed of the wall is $\Omega a/(\Phi\Omega) \approx 0.3$. This implies a lubrication layer must exist between the sphere and the wall. However, lubrication itself is not enough to provide the force necessary to keep the sphere away from the wall. This can be explained by the presence of a cavitation bubble which forms due to a local pressure drop, below the vapour pressure.

A heavy sphere is also investigated by Tagawa et al. [25]. In this work, another regime is described. When increasing the Reynolds number, the sphere goes from the fixed point by the wall, to the cascading regime described above, to a suspended regime. In this last regime, the sphere describes circular orbits.

Yang et al [26] consider the effects of roughness in the interactions of a heavy sphere with the cylinder wall, considering three roughened spheres and one smooth sphere. It is found that roughness does not have an effect on the size of the cavitation bubble that forms between the sphere and the wall or on the oscillatory regime described above. It was also found that the effect of roughness is significant only when the cylinder is rotating at speeds lower than 0.15 m/s. In this regime, the rough spheres suffered constant impacts with the cylinder wall, while the smooth sphere rotated constantly against the cylinder wall for all cylinder speeds.

Tooby et al. [27] studied the motion of a sphere immersed in a horizontally

rotating fluid. In this work, a wide range of density ratios $0.001 < P < 8.7$ was covered and the Reynolds number was adjusted to $Re = 10^{-2}$ to match that of diatoms in the ocean. Circular orbits were found consistently for all density ratios.

Studies on the motion of small air bubbles inside a horizontally rotating cylinder have been performed by Van Nierop et al. [28] and Lohse [29]. In this investigation, the bubble has an equilibrium position that is far from the axis of rotation of the cylinder. From this equilibrium position, the lift and drag coefficients were inferred.

A similar study on drag and lift forces experienced but for a solid sphere immersed in a horizontally rotating flow can be found in the work of Bluemink et al [30]. In this work, a wide range of Re is explored by using different mixtures of glycerol and water, and in all cases the sphere is lighter than the fluid. The results reported here show that an equilibrium position is found for the more viscous cases, when the mixture has 60% of glycerol or higher and $20 < Re < 30$.

In another investigation by Bluemink et al. [31] it was found that the rotation rate of a solid sphere immersed in a horizontally rotating flow can be higher than the rotation rate of the cylinder itself and the surrounding fluid for $2 < Re < 50$. This may suggest there is an alteration in the vortex structure of the wake left by the sphere, because it is observed that the effect increases with the Reynolds number, as the strength of the vortex does.

There are also studies made on heavy cylinders inside of a horizontally rotating cylindrical drum filled with water with $2500 < Re < 25000$ by Sun et al. [32] and Seddon et al. [33] who found an unexpected phenomena; a heavy cylinder rotating by the wall of the drum can counter-rotate with respect

to the wall of the drum. A chain of cavitation bubbles was found in the lubrication layer between the cylinder and the wall, controlling the direction of rotation of the cylinder. This shows that the cylinder does not correspond to a 2 dimensional version of the sphere problem. Moreover, the cavitation bubble chain is an example of the importance are three-dimensional effects in this case.

The motion of heavy ellipsoids immersed in a horizontally rotating flow has been studied by Seddon et al. [34] with focus in the regimes when the ellipsoid is next to the wall of the drum. The motion of the ellipsoid is highly dependent on their maximum curvature with respect to the radius curvature of the cylinder. If the maximum curvature of the ellipsoid is smaller than the curvature of the cylinder, the motion is consistent, with the axis of the ellipsoid aligned with the axis of rotation of the drum. No cavitation is bubble is found in this case. If the curvature of the ellipsoid is the same as the cylinder, the axis of the ellipsoid is also aligned with the drum for a wide range of Reynolds numbers. However, if the maximum curvature of the ellipsoid is larger than the curvature of the wall, the ellipsoid lies tilted by the wall, which gives rise to a tangential force that causes the ellipsoid to travel from one end of the drum to the other.

1.4 Theoretical Background

The problem of modelling the dynamics of a sphere immersed in a rotating viscous flow can be formulated in two different ways. The first one is to assume the Reynolds is infinitely small and the sphere's size tends to zero, so the equations governing the dynamics of the sphere are Stokes equations. The

second one is to assume that the Reynolds number and the size of the sphere are small but finite. Under these assumptions, a more complex formulation arises. Below, these two approaches and the conclusions drawn from them are reviewed.

1.4.1 A Sphere Immersed in a rotating Stokes Flow

The Stokes approximation corresponds to a reduction of the full Navier-Stokes equations when considering that the viscous effects are much bigger than the inertial effects [35]. The homogenous Stokes equations for the velocity of the fluid $\vec{u}$ are:

$$\mu\nabla^2\vec{u} - \nabla p + = 0, \tag{1.5}$$

$$\nabla \cdot \vec{u} = 0, \tag{1.6}$$

where p corresponds to the dynamic pressure field and μ is the dynamic viscosity which is $\rho_g\nu$. Equation 1.6 is the incompressibility condition

It is relevant to note that the homogenous Stokes equations are: linear, reversible and time independent (no history forces) [3], which simplifies the formulation greatly.

In the work of Lee and Ladd [36] a Stokesian calculation of the forces acting on a point-like particle immersed in a rotating Stokes flow are: the gravitational forces (weight and buoyancy), the centripetal force and the viscous forces. The forces acting over a sphere at a distance $\vec{r}$ from the centre of rotation of the flow that has an angular velocity Ω is given by:

$$\vec{F} = m_B\vec{g} + m_B\Omega^2\vec{r} = \xi[\vec{u} - \vec{u}(\vec{r})], \tag{1.7}$$

for a sphere at a distance $\vec{r}$, m_B is the buoyancy-corrected mass defined as $m_B = \frac{4}{3}\pi a^3(\rho_g - \rho_s)$, $\xi = 6\pi\nu\rho_g a$ is the friction coefficient, $\vec{u}$ is the velocity of the sphere and $\vec{u}(\vec{r})$ is the velocity of the fluid at distance $\vec{r}$.

Solving for $\vec{u}$ in polar coordinates it can be found that

$$u_r = u_s\left(\frac{r}{D_1 a} - \sin\theta\right) \tag{1.8}$$

and

$$u_\theta = u_s\left(\frac{r}{D_2 a} - \cos\theta\right), \tag{1.9}$$

where $D_1 = \frac{g}{\Omega^2 a}$ and $D_2 = \frac{u_s}{\Omega a}$ are dimensionless numbers and $u_s = m_B g\xi^{-1}$.

An equilibrium position can be found if u_r and u_θ are equal to zero. Using $\Omega = 1$ to calculate where this fixed point would be, it was found that the angle would be $\theta = 5.7 \times 10^{-4}$ and $r = 20$ mm. But this equilibrium was found to be unstable. A particle placed near it would spiral outwards and eventually collide with the walls of the container.

1.4.2 Finite Reynolds Calculations

In the work of Magnaudet [37] the forces acting over bubbles and rigid particles, moving in an unbounded flow, are reviewed for low to moderate Reynolds numbers. Here is stated that the forces acting on a rigid sphere are: the buoyancy force, the steady drag, the Basset's history force [38], [39], the added mass effect and the lift force by Saffman [40], [41], and extended by McLaughlin [42].

However, in the case of a light sphere immersed on a rotating fluid at low but finite Reynolds, the relevant forces are: a centripetal force, with a correction due to the added mass effect, the buoyancy force and the drag force, which is modified. A scheme of all the forces acting on a sphere immersed in a viscous flow is shown in figure 1.4. Moreover, in the work of Gotoh [43] the drag force is calculated have two components, an azimuthal component, as the steady drag and a radial component due to the curvature of the base flow. The radial component of this force, calculated by Gotoh is a centripetal force, which is much more significant than the other radial forces that could be considered in this regime (like the Saffman's lift force).

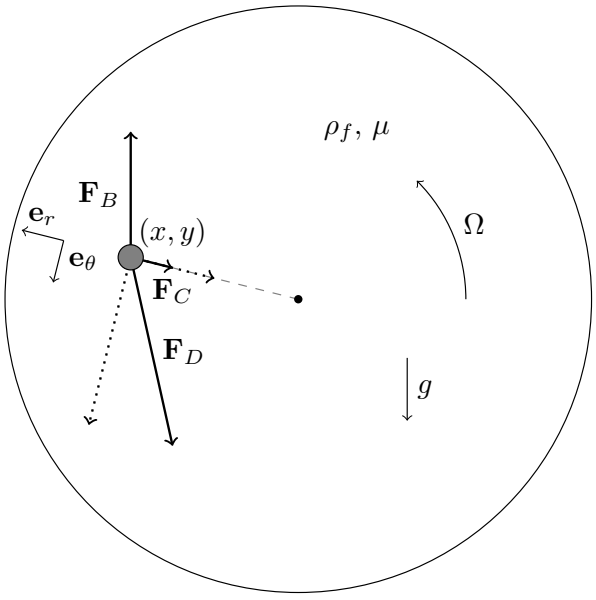

Figure 1.4: Schematics of the forces that a sphere experiences when immersed in a rotating fluid by Chris Johnson [44]. F_B is the sum of weight and buoyancy, F_C is the centripetal force and F_D is the drag force.

In the work of Van Nierop et al. [28] a physical argument is made to explain this difference. For low-Re the lift force has two components. The

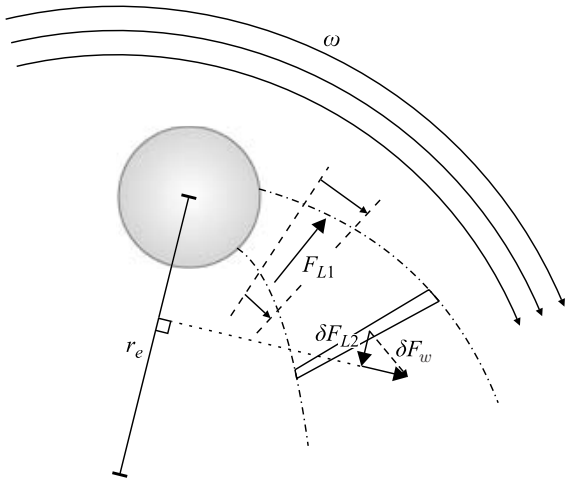

Figure 1.5: Schematics of the lift force induced by the wake on a sphere immersed in a rotating flow by Van Nierop et al. [28], F_{L1} is analogous to Saffman's lift and F_{L2} is the radial component of the force induced by the wake F_ω

centrifugal component F_{L1}, analogous to Saffman's lift [41] , is due to the linear increase of the velocity of the base flow with the radius. The velocity difference between the base flow and the defect speed in the wake, is greater on the outer side of the wake than in the inner side. The consequence of this effect is the centrifugal lift force F_{L1} shown in figure 1.5.

The centripetal component is due to the curvature of the wake, that follows the base flow. An infinitesimal slice of the wake results in a force δF_ω, perpendicular to the plane of the slice and pointing downstream as shown in figure 1.5. The total force induced by this effect $F_\Omega = \int \delta F_\omega$ results on a drag force which azimuthal contribution corresponds to the centripetal force F_{L2}. The work of Gotoh [43], that consist on a complete theoretical calculation of the transverse force acting on a sphere fixed in a rotating flow, indicates the centripetal component of the aforementioned lift is the dominant component.

It is important to note that up to the development of the theoretical model utilised in this thesis, no theoretical model was available to compare the experimental results obtained in this thesis work.

Numerical studies have been done on this flow configuration by Mukundakrishnan et al. [45]. They performed direct numerical simulations (DNS) for the complete Navier-Stokes equation for an incompressible fluid, considering a horizontal rotating cylinder which is finite for $1 < Re < 60$. They reported that, when running their simulations for $Re = 3$, $Re_p = 56$ and $P = 0.8$, a light particle has a stable fixed point.

1.5 Thesis Structure

This thesis is structured as follows:

In chapter §2 the experimental apparatus used to investigate the motion of a positively buoyant sphere immersed in a viscous flow is presented. The calibration of the motor used to generate the rotation is shown, the spheres used in the investigation are described and the data acquisition and processing is outlined. The measurements for the terminal velocity of the spheres are also presented.

The experimental measurements of the equilibrium position of the sphere and its dependance on the size of the spheres are presented in §3. A theoretical model for the equilibrium position is developed and compared with the experimental data. The stability of the fixed points and their dependance on the radius of the sphere is discussed.

The experimental measurements of the limit cycle that arise from the instability of the equilibrium position are presented in chapter §4. This

limit cycle has the form of periodic circular orbits, and the dependance of the orbital radius is studied as a function of the Reynolds number Re. In this chapter another limit cycle is described: the oscillatory motion that the sphere undergoes when it is close to the wall of the cylinder.

In chapter §5 the behaviour of a hollow porous sphere, custom made for this investigation, is presented. The equilibrium position that this sphere finds and the orbital radius of the oscillations that arise from its instability are presented as a function of the Reynolds number Re. The instability of a hollow porous sphere oscillating by the wall of the cylinder is also presented.

In chapter §6 the study on equilibrium positions of spheres of different roughness is presented. The equilibrium positions of these rough spheres are compared with the equilibrium position of a smooth control sphere. The robustness of the fixed points is also discussed in this chapter.

Finally, in chapter §7 a summary of the work presented on this thesis is shown. Conclusions are drawn from the experimental results presented in this document and future experimental and theoretical work is suggested.

Chapter 2

Experimental Apparatus and Techniques

The experimental apparatus used to obtain a rotating viscous flow is described in this chapter. A complete description of the experimental parameters and data acquisition techniques are also outlined in this chapter.

In section §2.1 the experimental apparatus, used to obtain the rotating fluid, is described. The spheres used for this investigation are presented in section §2.2. Also, the fabrication process of the 3D printed spheres is described. In section §2.3 the properties of the working fluid are presented, and the experimental procedure to get rid of any air trapped in the fluid is described.

The data acquisition procedure, consisting of image acquisition, is outlined in section §2.4. In this section there is also a description of the image analysis procedure used to obtained the data from the images.

Finally in section §2.5 the measurements of the terminal velocity of the spheres used in this experiment are presented. The measured values are

corrected for wall effects and displayed in a table by the end of the chapter.

2.1 Experimental apparatus

The experimental apparatus comprised a precision bored right glass cylinder of length 225.000 ± 0.005 mm, inner diameter 120.000 ± 0.005 mm and a wall thickness of 5.200 ± 0.005 mm with ground ends custom made by Schott-Duram. A machined perspex cap was inserted in each end of the cylinder which were held by two machined aluminium rings and sealed by two o-rings. One cap contained a ball race and was positioned such that the surface cap was perpendicular to the inner wall of the cylinder. The cylinder was sealed using eight screws which held the aluminium rings together. With the bottom cap in place, the cylinder was filled with glycerol and a single sphere was placed inside it. The remaining cap, which had a ball race in its centre, was then placed at the other end of the cylinder and sealed using further aluminium rings and screws.

The cylinder was mounted horizontally between two bearings which engaged into the ball races such that the central axis of the cylinder was orthogonal to gravity. The apparatus was supported on a machined steel platform with three adjustable legs which were used to level the system.

The cylinder was rotated using a DC motor with feedback control (EW 4239 Servo Drive) via a $10 : 1$ gear box which was connected to the cylinder by a smooth belt. The speed of rotation was controlled by an external power supply which provided a voltage between $0 - 10$ Volts connected to a commercial servo control and the rotation frequency was measured using an optical shaft encoder. The optical shaft encoder produced 500 pulses per

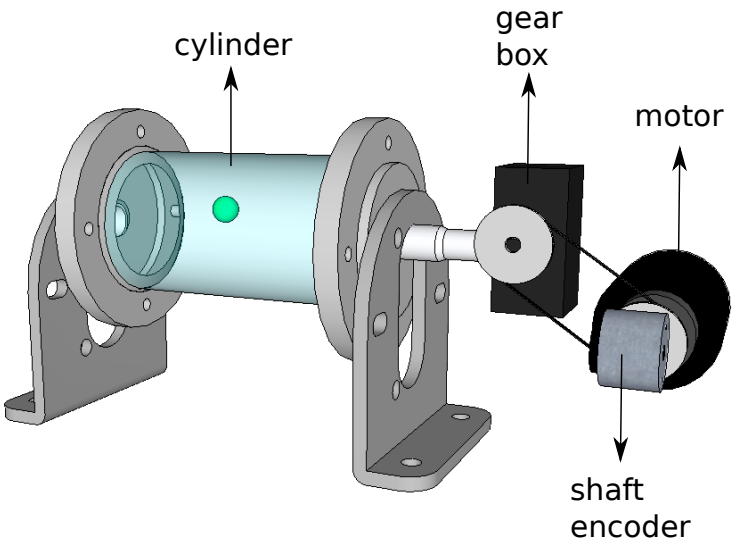

Figure 2.1: Experimental setup used to obtain a rotating viscous fluid: a glass cylinder completely filled with glycerol was placed with its axis perpendicular to gravity, a positively buoyant sphere was placed inside and the cylinder was rotated using a motor and a gear box. The frequency of rotation of the cylinder was measured using an optical shaft encoder.

revolution and was attached to the bearing shaft of the motor.

The frequency of the motor was measured using the readings of an universal counter which averaged every 100 measurements of the shaft encoder, and monitored by an oscilloscope to ensure the output signal corresponded to a square signal and that the shaft encoder was working correctly. This method was used to calibrate the rotation speed of the cylinder as a function of voltage applied to the motor, as shown in figure 2.2. Here, the angular velocity was proportional to the frequency measured by the universal counter $f_s = 500 f_{motor}$ and given the ratio of the gear box $f_{cylinder} = \frac{1}{10} f_{motor}$. We find $\Omega = 2\pi f_{cylinder}$ with an accuracy of $\pm 0.01\%$.

The Reynolds number considered in this system was defined as:

$$Re = \frac{a\Omega}{\nu}, \tag{2.1}$$

where a corresponded to the radius of the sphere, Ω to the angular velocity of the cylinder, and ν to the viscosity of the fluid.

The maximum angular velocity our motor could attain was $\Omega \approx 25$ rad/s meaning the maximum Reynolds number was $Re \approx 2$, but typical values used in the experiment were between $0.05 < Re < 1$. A schematic diagram of the experimental apparatus and the data acquisition instruments can be seen in figure 2.3.

Accurate levelling was essential, otherwise the effects of buoyancy would make the sphere slowly drift along the cylinder due to the buoyancy over long time scales. This typically took periods of hours and hence careful checks on the levelling were required using a precision engineer 's level which minimised this effect and the sphere would remain at a fixed position over 24 hours. Levelling was first performed on the platform and then on the

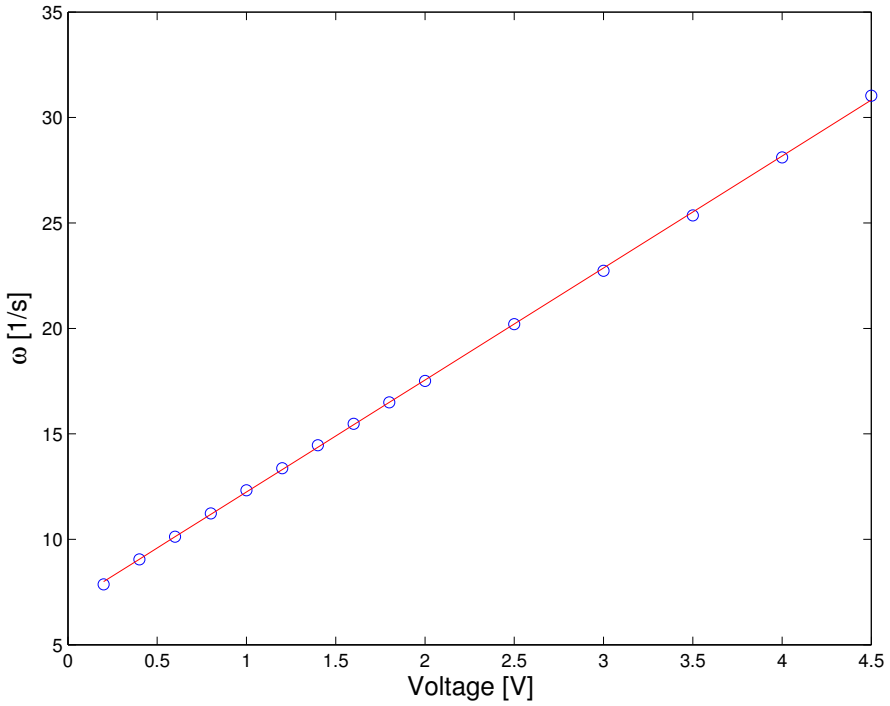

Figure 2.2: The angular velocity Ω of the cylinder plotted as a function of the input voltage, measured by an optical shaft encoder which sent 500 pulses per rotation to an universal counter. The universal counter measured a frequency $f_s = 500 f_{motor}$ and given the ratio of the gear box $f_{cylinder} = \frac{1}{10} f_{motor}$ finally $\Omega = 2\pi f_{motor}$

cylinder itself. Any small differences between the two sets of readings were accounted for using the adjustable feet. The cylinder with the sphere inside of it was next imposed a high acceleration reaching quickly a high rotation speed which drove the sphere to the centre of the cylinder. A pen mark was drawn over the central diameter of the cylinder marking its centre in the horizontal direction so the position of the ball could be checked compared to the centre of the cylinder. The cylinder was left to rotate for an hour,

which was enough time to measure small drifts of the sphere indicating an inclination of the rotational axis of the cylinder and was corrected for by levelling the cylinder accordingly.

All our experiments were performed in an air-conditioned laboratory in which the temperature was maintained at $20 \pm 0.5°$ C. A mercury thermometer placed next to the experiment monitored the temperature to ensure that it kept stable through out the entire process of the study which is of vital importance given that the kinematic viscosity of the glycerol changes approximately 9% within a temperature variation 1^{circ}.

2.2 Spheres

A variety of commercial and custom-made precision spheres were used on this investigation. Polypropylene spheres of density $\rho = 0.87 \pm 0.2$ g/cm^3 and radii $a = 3.15 \pm 0005$ mm, $a = 4.76 \pm 0.005$ mm, $a = 6.32 \pm 0.005$, $a = 7.05 \pm 0.005$ mm, $a = 7.90 \pm 0.005$ mm and $a = 9.50 \pm 0.005$ mm were used, all from Dejay distribution Ltd UK. The basic diameter tolerance given by the manufacturers for this spheres is of 0.02 mm. An image of this spheres is shown in section a) of figure 2.4. The manufacturing process for the polypropylene spheres meant that they could contain small air pockets, to check for the presence of bubbles, we cut open spheres of all the available sizes and only found bubbles in some of the spheres of radii $a > 7$ mm, and the bubbles found were never bigger than the 5% of the total volume.

In addition, several 3D printed spheres were produced. The 3D printing technique allowed us to create spheres of any size required for the experiment. This spheres were made of Stratasys ABSplus plastic which has a density of

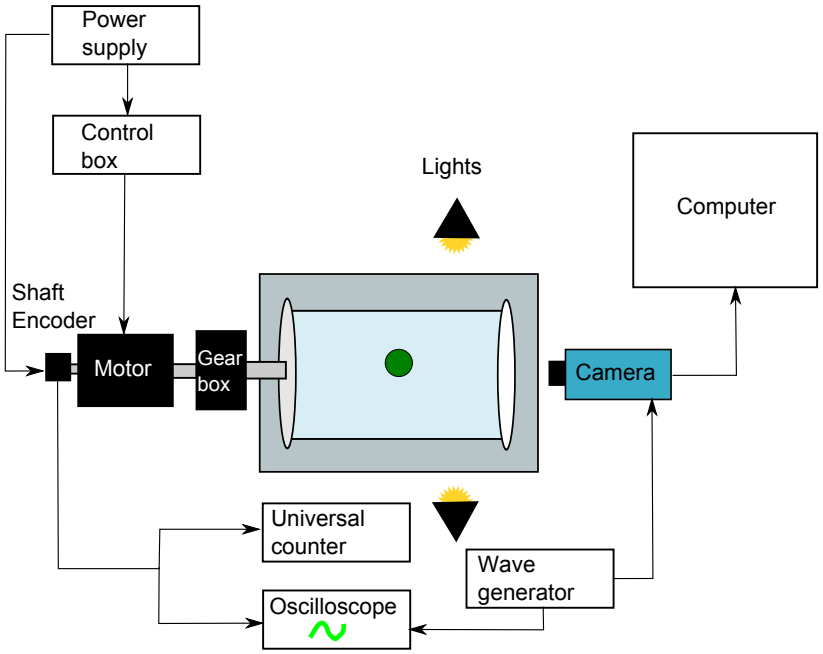

Figure 2.3: Schematic diagram of the experimental apparatus, a glass cylinder completely filled with glycerol was placed over an adjustable platform. The cylinder was driven by a motor connected to a gear box and the frequency of the rotation was measured by an optical shaft encoder attached to the bearing end of the motor. The motor was driven by a feedback controlled supply which was connected to a power supply. The back lid of the cylinder was painted black or white and the front lid was transparent. A camera controlled by a computer acquired images from the front of the cylinder. The acquisition frequency of the camera was set using a wave generator. An oscilloscope monitored the output of he shaft encoder and the wave generator.

a)


b)
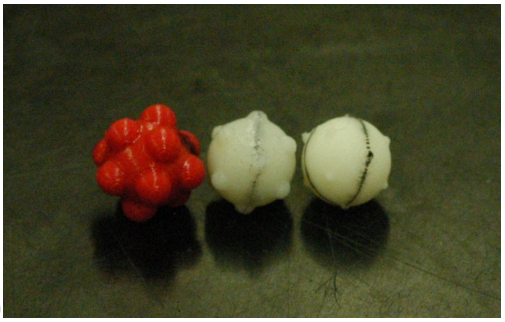

c)
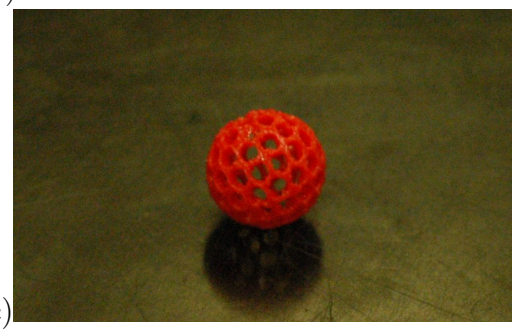

Figure 2.4: *a)* polypropylene spheres of the different sizes using, here, the radii ranged from 9.50 mm to 3.15 mm . *b)* Spheres with different roughness made by the 3D printing technique, the inner radius for the three of them was 6 mm and the outer radius are 8, 7 and 6.5 mm respectively. *c)* Hollow porous sphere made in our 3D printer of 8 mm of radius.

$\rho_{plastic} = 1.04$ g/cm^3. A plastic thread of 1.8 mm of diameter was injected through a heated nozzle of 0.35 mm, the heat partially melts the plastic and it becomes flexible enough to be deposited in lines creating a layer of material. When a layer was finished, the 3D printer displaces the printing surface and

prints another layer on top of the previous one. The displacement between layers can be adjusted between $0.18 - 0.25$ mm.

As a consequence of the manufacturing process, very small air bubbles, with radius of the order of the separation between layers, could be randomly distributed inside of the 3D printed spheres

To ensure a consistent density through all the experiments performed with 3D printed spheres, the spheres were saturated with fluid removing all the air trapped inside of them as a result of their fabrication. To do this, the sphere was weighed down inside of a beaker filled with glycerol and then the air trapped was removed with a vacuum pump before placing it inside the cylinder. The measured density of the spheres when completely saturated with glycerol was $\rho_s = 1.17$ g/cm^3. This process delivered completely isotropic spheres.

3D printing also allowed to fabricate spheres specifically designed to study the effect of roughness in this system. Spheres with 10 uniformly distributed hemispherical bumps on the surface were produced in this way. The spheres were characterised by their inner and outer radius; the inner radius was always $a_{min} = 6$ mm and the outer radii were $a_{max} = 6.5$ mm, $a_{max} = 7$mm and $a_{max} = 8$ mm. We also made a sphere of radius $a = 7mm$ as a control sphere without bumps, to compare against any results obtained with the rough spheres. This spheres are shown in the section b) of figure 2.4.

Given that one of the motivations of this work was the resemblance of this geometry to tissue growth engineering, a hollow sphere of a radius of $a = 8$ mm with holes in its surface was fabricated using the 3D printing technique as shown in section c) of figure 2.4. This sphere resembles the porosity of a biological scaffold which interchanges nutrients with the surrounding fluid

Figure 2.5: Suspended level viscometer used to measured the viscosity of the glycerol at lab temperature $T = 20 \pm 0.5^{\circ}$ C

[46].

The porous sphere had a typical pore size of 2 mm and a weight of 0.436 g. The density of this sphere when dry was 0.2033 g/cm^3, but it needs to be taken into account that when this sphere is immersed in fluid, there is also fluid inside.

Light pen marks were applied, marking two perimeters of each sphere in such a way that the two lines would cross in two diametrically opposed points. This lines allowed us to follow the rotation of the sphere over time. This pen marks did not affect the dynamics of the sphere.

2.3 Working Fluid

The working fluid in the experiment was glycerol supplied by Sigma-Aldrich chemicals. The density of the fluid was verified using an accurate digital balance to measure the weight of a known volume and hence confirm the density of the glycerol. The density obtained from this measurement was $\rho_g = 1.261$ g/cm^3 at 20 °.

The viscosity of the glycerol was measured using a suspended level (Ubbelohde) viscometer at a temperature of $T = 20 \pm 0.5°$ C and had a value of $\nu = 1100.9$ mm/s^2 with an accuracy given by the manufacturer of 0.28 %. The viscometer is shown in figure 2.5. The glycerol was kept in sealed containers at all times to avoid water absorption from the environment.

A practical difficulty which was encountered in the experiment was that air bubbles became trapped in the fluid during the filling process. Dissolved air could also be released by the glycerol. The method we developed to deal with this issue was to rotate the cylinder at high speeds, this drove the air bubbles to the central axis of the cylinder where they merged forming bigger bubbles. These bubbles were then easily removed using two small sealable holes in one of the lids of the cylinder, through one of the holes we injected glycerol, using a syringe, that had been previously degassed using a vacuum pump, in the cylinder which pushed the bubbles out through the other hole.

2.4 Data Acquisition

2.4.1 Images

To measure the position of the spheres, images were taken from the front of the cylinder using a high speed camera (pco.1200 hs) with a spatial resolution of 1280x1024 pixels. To avoid undesired shadowing, the cylinder was illuminated from both sides using two incandescent light sources.

The back lid of the cylinder was painted white or black, depending on the colour of the sphere to be investigated. A white screen was preferred when green and red spheres were used, because it ensured a good contrast between the background and the sphere, while a black screen was used when measuring white spheres.

Images were captured with the camera connected to a computer which has a dedicated software for image acquisition. The shutter of the camera was controlled using a square wave generator, the width of the generated pulse determined the shutter speed of the camera while the period of the wave determined the frame rate of the camera. There was a compromise between spatial resolution and the range of movement of the sphere that could be sampled depending on our choice of camera lenses. The chosen resolution of the camera was approximately 10 pix/mm using lenses of focal length 50 mm.

Matlab scripts were developed to track the centre of the spheres and determine its position in consecutive images using the greyscale in the images. In this way the position of the sphere was tracked and it was possible to reconstruct the movement of the sphere over the time series acquired.

The position of the pen marks over the sphere were tracked along an image

sequence recorded at a fixed Reynolds number. The difference in position for a given time step results in a measurement of the angular speed of the sphere.

2.5 Terminal velocity

The terminal velocity corresponds to the steady velocity that a rising object reaches when it is released in an infinite container full of fluid and the forces acting on the object: buoyancy, weight and drag, balance. Leaving the object to rise with zero acceleration.

The terminal velocity was an important parameter to enable a comparison between the theory and experiment in this work and it is [47]:

$$V_T = \frac{2ga^2(\rho_g - \rho_s)}{9\rho_g \nu}, \tag{2.2}$$

this expression is valid for rigid ideal spheres in an infinite container. Considering that this study also comprises not only real spheres, but also rough spheres and a porous sphere, this parameter needed to be measured experimentally, a comparison with the theoretical value is provided at the end of this section.

The sphere was placed in a trap at the bottom of a cylindrical beaker of $D = 280$ mm of diameter and $H = 425$ mm of height. The trap consisted of a small beaker glued to the bottom of the big one using double sided tape and a sliding aluminium lid which was attached to a piece of string that could be pulled from the outside to release the sphere. The beaker was filled with glycerol to a depth of 280 mm. As a consequence of the filling process, air bubbles became trapped in the fluid. To remove them, the experiment was

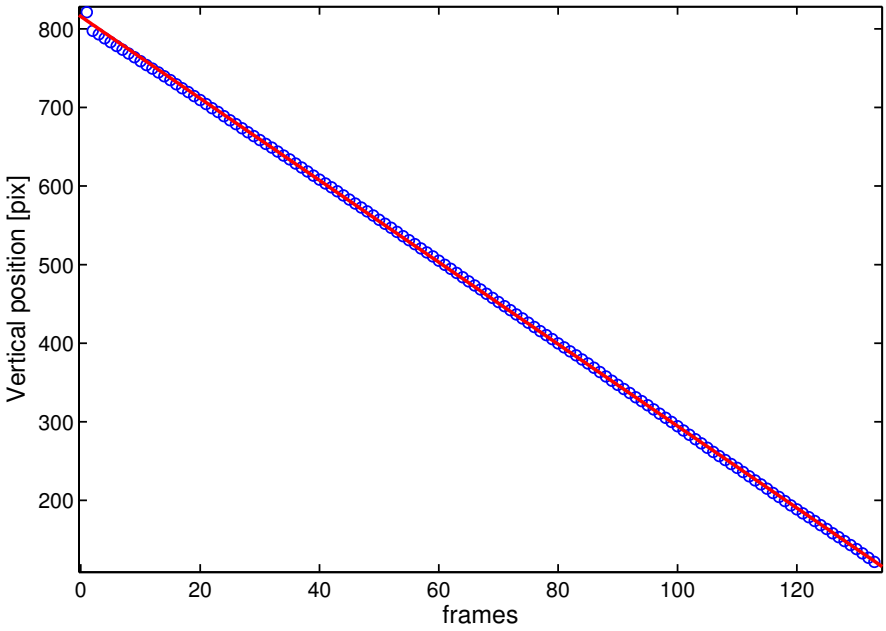

Figure 2.6: Position of a sphere of $a = 7.90$ mm plotted as a function of time and a linear fit that allows to estimate the terminal velocity.

left to rest for 2 days so all the bubbles floated to the surface. A lid was placed on the beaker during this process to avoid thinning of the fluid due to water from the atmosphere getting dissolved in the glycerol.

A single sphere was released from the trap and its trajectory was recorded by the camera at 50 fps. An exception was made for the porous sphere, which trajectory was recorded at 10 fps because the rising speed was much slower than in the solid sphere cases. An example of the position of the sphere plotted as a function of time is shown in figure 2.6. Here the vertical position is measures from the top of the frames, which is why it decreases with time when the sphere is rising.

The beaker had a circular cross section, which distorted the images in the horizontal direction. Therefore, the conversion factor from pixels to mm was calculated by measuring the diameter of the sphere in the vertical direction in the recorded images.

The position of the sphere at each time of the image sequence was determined by a dedicated Matlab script. In figure 2.6 the time evolution of the vertical coordinate of a sphere of $a = 7.9$ mm is shown. A linear fit of allows to estimate the experimental terminal velocity for each sphere and the error of the measurement was given by the error on the fit.

Because the theoretical terminal velocity V_T is calculated for a sphere moving inside an infinite container and the experiment was performed in a finite beaker, is necessary to take into account the effect of the walls on this measurement, the effect of the finite length of the beaker is considered to be negligible. The aspect ratio between the biggest sphere used in this study and the beaker was $\frac{a}{D/2} = 0.0679$ and the Reynolds number was $Re_p = \frac{aV}{\nu} < 0.01$.

In the work of Fidleris and Whitmore [48], wall effects on the terminal ve-

locity for falling spheres for an extensive range of aspect ratios and Reynolds number were studied. They compared the different corrections available on the literature for the measured velocities, with the velocity of particles falling in an infinite fluid and conclude that for different aspect ratios and Reynolds number, different corrections need to be taken into account. Particularly, for the Stokes'-flow region ($Re < 0.2$) and small aspect ratio ($0 < 2a/D < 0.4$) the best correction factor was the one given by Francis [49]:

$$v_\infty = v\left(\frac{1-(2a/D)}{1-0.475(2a/D)}\right)^{-4}, \tag{2.3}$$

where v corresponds to the measured velocity of a container of diameter D and v_∞ corresponds to the terminal velocity, for an infinite container.

In table 2.1 the measured terminal velocities are presented for all the spheres to be considered in this study. The corrected speeds due to the effects of the walls using the correction factor of equation 2.3 are displayed as $V_{Tcorrected}$, the error shown here was propagated from the error in V_T, which is not displayed. The theoretical values for the terminal velocity are also shown. Nevertheless, the values to consider in this study are $V_{Tcorrected}$.

The experimental values of the terminal velocity for the rough spheres show that roughness has an effect on the terminal velocity, decreasing it when increasing the roughness. This can be explained due to the increase drag that a rougher sphere experience in comparison with a smoother one.

The theoretical value for the porous sphere was calculated using its weight when dry $W_d = 0.436$ g and the known density of the plastic used by the 3D printer to calculate the volume fraction used by plastic and glycerol, doing so an effective density was calculated to be $\rho_p orous = 1.244$ g/cm^3.

With this values of the terminal velocity, Re_p goes from 0.0512 for the

Polypropylene spheres radius [mm]	V_T [m/s]	$V_{Tcorrected}$ [m/s]	$V_{T_{theory}}$
4.78	0.0180	0.0187 ± 0.00005	0.0140
6.33	0.0351	0.0387 ± 0.00005	0.0246
7.90	0.0446	0.0474 ± 0.00005	0.0383
9.50	0.0630	0.0678 ± 0.00005	0.0554
Rough spheres outer radius [mm]			
6.5	0.0200	$0.0221pm0.00005$	0.0055
7.0	0.0189	0.0211 ± 0.00007	0.0060
8.0	0.0177	0.02006 ± 0.00001	0.0069
Porous sphere 8 mm			
8	0.0055	0.0062 ± 0.00008	0.0016

Table 2.1: V_T correspond to the terminal velocities for all the spheres under this study, $V_{T_{corrected}}$ correspond to the corrected terminal velocities considering wall effects and $V_{T_{corrected}}$ to the terminal velocity given by the theory.

porous sphere, to 0.384 for the biggest polypropylene sphere.

Chapter 3

Fixed points

In this chapter the positions of equilibrium which arise when a positively buoyant sphere is immersed in a cylinder where the axis of rotation is horizontal are examined.

In section §3.1 a theoretical model is developed. In this model, the forces acting on the sphere are considered and the positions of equilibrium are calculated.

The experimental results for the average position of spheres of different radii as a function of the Reynolds number are reported in section §3.2.

In section §3.3 the theoretical predictions given by the model presented in section §3.1 are compared with the experimental results presented in section §3.2.

In section §3.4 the stability of the fixed points and their dependance on the radius of the spheres is discussed.

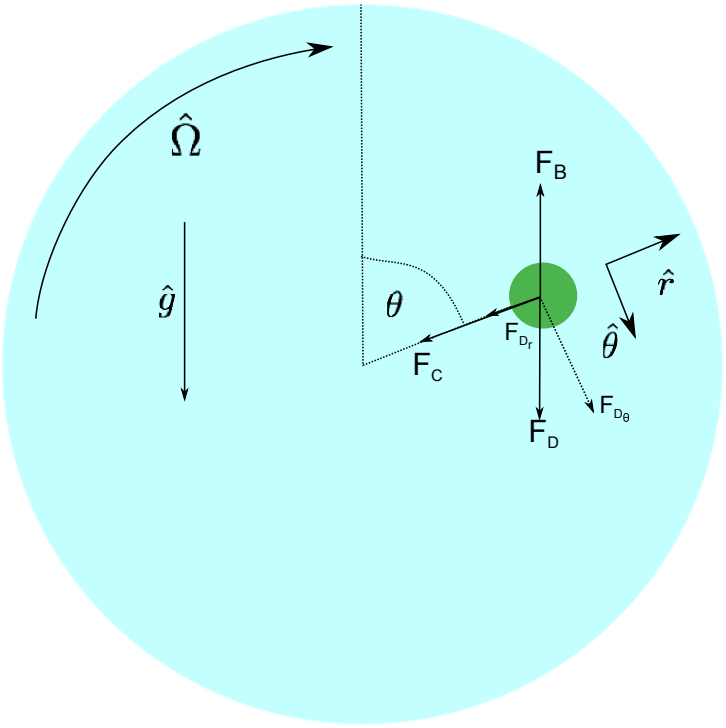

Figure 3.1: Schematic diagram of the forces acting on a light sphere immerse in a horizontally rotating viscous flow, $\hat{r}$ and $\hat{\theta}$ depict the radial coordinate system used to describe the forces, Ω corresponds to the angular velocity of the fluid, g to the acceleration of gravity, F_B corresponds to the sum of the buoyancy and the weight of the sphere, F_C to the centripetal force and F_D to the viscous drag which is decomposed in its radial and azimuthal components F_{D_r} and F_{D_θ}

3.1 Theory

The following theoretical model was developed by Chris Johnson [44]. The system considered is an infinitely long cylinder of radius R filled with a fluid of viscosity ν and density ρ_g, which is rotating with the axis of rotation orthogonal to gravity. A positively buoyant sphere of radius a and density ρ_s is immersed in the fluid. A schematic diagram of all the forces involved is shown in figure 3.1.

A polar coordinate system is used, which is represented here by the unit vectors $\hat{r}$ and $\hat{\theta}$. The angular velocity of the fluid in this coordinate system is given by $\vec{\Omega} = \Omega\ \hat{\theta}$ and the acceleration of gravity is $\vec{g} = -g(\hat{\theta}\cos\theta + \hat{r}\sin\theta)$. The cartesian coordinates x and y are described in terms of the radial and azimuthal coordinates are $x = r\cos\theta$ and $y = r\sin\theta$. From the aforementioned dimensional parameters we define three non dimensional quantities: the shear Reynolds number Re

$$Re = \frac{a^2\Omega}{\nu}, \tag{3.1}$$

and the particle Reynolds number

$$Re_p = \frac{aV_T}{\nu}, \tag{3.2}$$

where

$$V_T = \frac{2ga^2(\rho_g - \rho_s)}{9\rho_g\nu}, \tag{3.3}$$

is the terminal velocity of a positively buoyant sphere rising in a viscous fluid.

3.1.1 Balance of Forces

The forces acting over the sphere are shown in the schematic diagram presented in figure 3.1. The vertical forces, buoyancy and weight of the sphere can be written in the form:

$$\vec{F_B} = \vec{g}(\rho_g - \rho_s)\frac{4}{3}\pi a^3, \tag{3.4}$$

the centripetal force, which acts on the radial direction, and

$$\vec{F_C} = -\frac{3}{2}\cdot\frac{4}{3}\pi a^3 \Omega^2 r \rho_g \hat{r}, \tag{3.5}$$

where the factor 3/2 arises from the added mass of Maxey and Riley [50].

At small Reynolds number ($Re_p \ll Re^{1/2} \ll 1$), the leading contribution of inertia is an adjustment to the Stokes drag calculated by Gotoh [43] as:

$$\vec{F_D} = 6\pi\nu\rho_g a r\Omega[(1 - k_1 Re^{1/2})\hat{\theta} - k_2 Re^{1/2}\hat{r}] + O(Re), \tag{3.6}$$

where

$$k_1 = 3\frac{\sqrt{2}(19 + 9\sqrt{3})}{280} \simeq 0.524, \tag{3.7}$$

and

$$k_2 = 3\frac{\sqrt{2}(19 - 9\sqrt{3})}{280} \simeq 0.0517. \tag{3.8}$$

are the correction factors calculated by Gotoh [43] due to the curvature of the base flow, such that $\vec{F_D}$ also contains azimuthal and radial components, $F_{D\theta}$ and F_{Dr} which are drawn in solid lines in figure 3.1. This corrections result in an increased drag and the radial component corresponds to a lift force, that points towards the centre of rotation.

The sphere will be in equilibrium if the balance of the azimuthal and radial components of the forces is equal to 0. This means that the azimuthal component of the drag force $F_{D\theta}$ must balance the azimuthal component of the buoyancy force $F_B \cdot \hat{\theta}$ and the radial component of the drag force F_{Dr} with the radial component of the buoyancy $F_B \cdot \hat{e_r}$, must balance the centripetal force F_C This provides the condition for an equilibrium position that can be written in cartesian coordinates as:

$$x = r\cos\theta = -a\frac{Re_p}{Re}\frac{1 + k_1 Re^{1/2}}{(1 + k_1 Re^{1/2})^2 + Re(k_2 + \frac{1}{3}Re^{1/2})^2} \tag{3.9}$$

and

$$y = r\sin\theta = a\frac{Re_p}{Re^{1/2}}\frac{k_2 + \frac{1}{3}Re^{1/2}}{(1 + k_1 Re^{1/2})^2 + Re(k_2 + \frac{1}{3}Re^{1/2})^2}. \tag{3.10}$$

.

The predictions of the model will be compared with the experimental results later in this chapter.

3.2 Experimental results

3.2.1 Average position

For spheres of different radii, an image sequence of 120 frames was recorded, and the position of the centre of the sphere was measured for each image, then an average of this positions was calculated as a function of the Reynolds number.

A single sphere was placed inside of the cylinder and the rotation velocity

was set to a maximum of approximately 20 rad/s. The speed of rotation was decreased by small steps ($\Delta\Omega \approx 1$ rad/s) and a sequence was recorded.

Two time scales were considered when taking into account how long it took to the fluid to achieve solid body rotation after the rotational velocity has been modified. The work of Greenspan and Howard [51], describes that the viscous diffusion time can be calculated for our system as

$$T_1 = \frac{R^2}{\nu} \simeq 3.2 \quad sec, \tag{3.11}$$

and the spin up time can be calculated as:

$$T_2 = \sqrt{\frac{R^2}{\nu\Omega_{spin}}} \simeq 1.8 \quad sec. \tag{3.12}$$

In both cases R corresponds to the radius of the cylinder, ν to the viscosity of the glycerol and $\Omega_{spin} = 1$ rad/s to the change in angular velocity which has been imposed.

To ensure the fluid inside the cylinder was set in solid body rotation, a time much longer than T_1 and T_2 was allowed for all perturbations to settle between the measurements. The time between measurements was monitored by a stopwatch and the experiment was left for at least 2 minutes between experiments.

An image sequence was recorded at 20 frames per second with the fast camera for a fixed rotation velocity to obtain the average position of the sphere at a given Reynolds number. Then the rotation velocity was reduced in small steps, by reducing the voltage in the power supply controlling the motor, until the desired velocity was reached and the system was let to settle before recording the next image sequence.

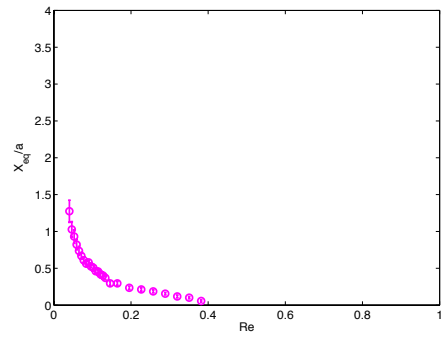

(a) $a = 4.75$ mm

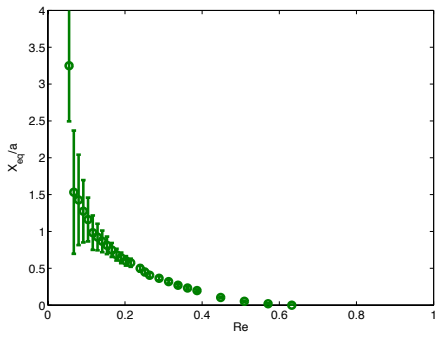

(b) $a = 6.33$ mm

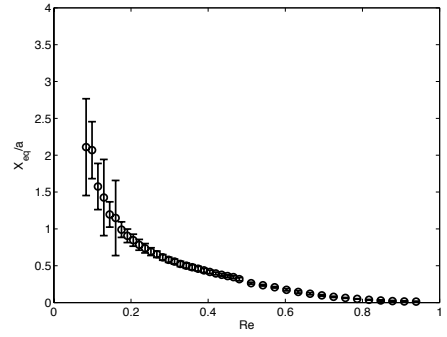

(c) $a = 7.05$ mm

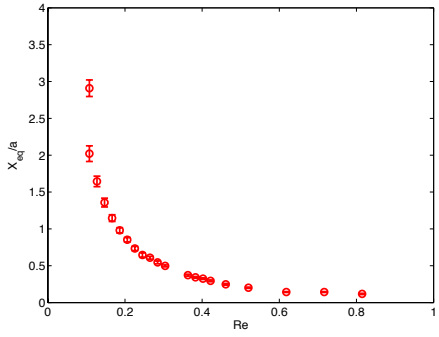

(d) $a = 7.90$ mm

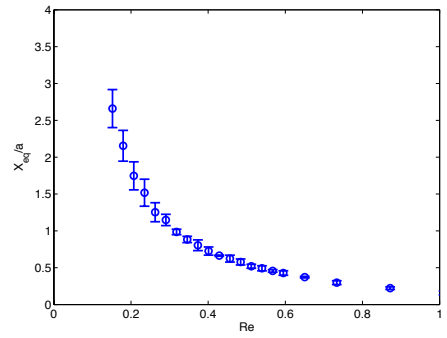

(e) $a = 9.05$ mm

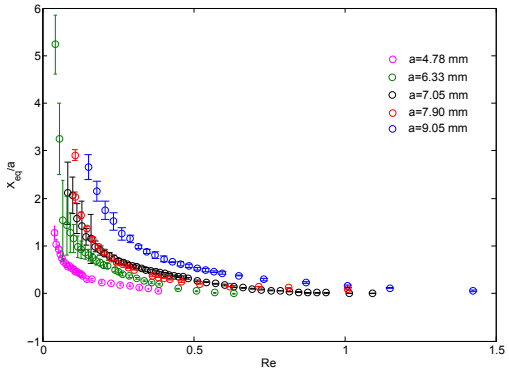

(f) all radii

Figure 3.2: Average position of polypropylene spheres of radii $a = 9.05$, 7.90, 7.05, 6.33, 4.78 mm. The error bars in this plot correspond to the standard deviation from the average position

In figure 3.2 the average position X_{eq}, measured from the central axis of the cylinder is shown plotted as a function of the Reynolds number for all the polypropylene spheres under this study.

The average position is normalised by the radius of the corresponding sphere.The error bars in this plot correspond to the standard deviation from this average and it can be noticed that the standard deviation grows with decreasing Reynolds number for all of the studied spheres. This is not due to a larger experimental error, instead, it indicates where the sphere began to oscillate such that its centre moved in a circular orbit below a threshold Re_c. Hence the size of the error bar corresponds to the diameter of the circular orbit.

In figure 3.2 (a) the normalised average position of a sphere of radius $a = 4.75$ mm is shown plotted against the Reynolds number in magenta, This was the smallest sphere considered in this study and as it can be seen from the size of the error bars, it was also the most unstable.

In figure 3.2 (b) the normalised average position of a sphere of radius $a = 6.33$ mm is shown plotted against the Reynolds number in green. In this case, there is a clearer threshold from where the sphere starts oscillation when looking at the error bars.

In figure 3.2 (c) the normalised average position of a sphere of radius $a = 7.05$ mm is shown plotted against the Reynolds number in black. It can be observed that the range when the error bars are increases in size considerably in comparison with the previous cases.

In figure 3.2 (d) the normalised average position of a sphere of radius $a = 7.90$ mm is plotted against the Reynolds number shown in red. This case is very similar to the one in section (c) due to the similarity in the radius of

the spheres considered.

In figure 3.2 (e) the normalised average position of a sphere of radius $a = 9.05$ mm is plotted against the Reynolds number shown in blue. this is the biggest sphere in this study, it can be observed how the range of small error bars, indicating that the sphere is on a fixed point, is much larger than in previous cases.

In figure 3.2 (f) the normalised average position of all spheres is plotted against the Reynolds number, from this plot it can be seen that the average position depends on the size of the sphere. This figure also suggest that the functional dependence of the average position on the Reynolds number has to be the same for all the spheres under this study.

In the next section a comparison between the model and the experimental data presented here is discussed.

3.3 Comparison with the Model

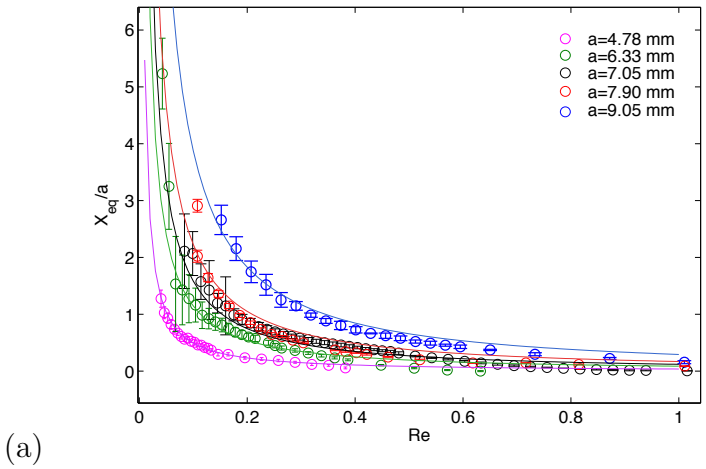

(a)

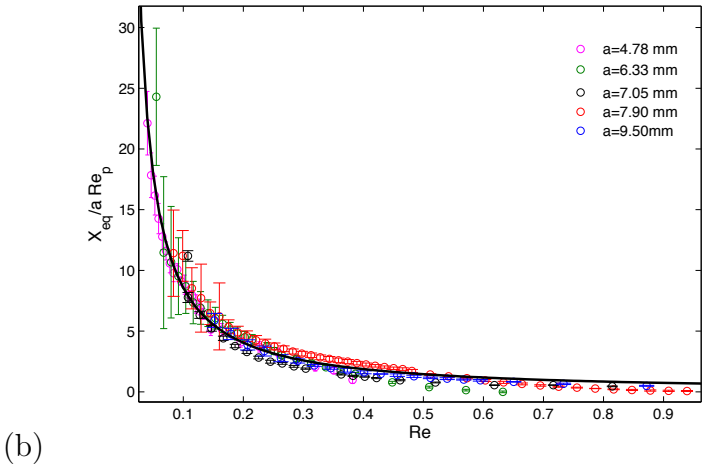

(b)

Figure 3.3: (a) Average position of the spheres X_{eq}, the solid line shows the theoretical model for each sphere. (b) Average position of the sphere normalised by aRe_p , this normalisation produced a collapse of the experimental data. The black solid line shows the theoretical model

In order to compare the experimental results with the theoretical model for the equilibrium position X_{eq} introduced previously in this chapter, the theoretical curve given by 3.9 is plotted together with the measured experimental

data in figure 3.3. In section (a) of figure 3.3 the average position non dimensionalized by the radius of the sphere is shown. In section (b) of figure 3.3, the collapse of the data when non dimensionalized by aRe_p is shown. The normalisation chosen for section (b) was chosen considering that Re_p is proportional to X_{eq} as shown in equation 3.9. This normalisations results in a good collapse of the data.

In both cases the solid lines corresponds to the theoretical curve, illustrating that the agreement of the model with the data is very good, particularly for small Reynolds number. For $Re > 0.5$ the model deviates slightly from the experimental data, this is because the model was calculated for the limit of very low Reynolds.

A displacement in the vertical direction, above the horizontal mid-plane of the cylinder, is also predicted by the model as stated in equation 3.10, but this displacements were below the experimental resolution of this setup.

Moreover, using the parameters of our experiment in the model, it can be seen how these displacements are very small compared with the displacements in the horizontal direction. The model predicts a maximum displacement in the y direction of $Y_{eq} = 0.68$ mm for the biggest sphere in this study, of radius $a = 9.50$ mm, considering $Re = 0.1$ while for the same set of values the theory predicts a displacement in the x direction of $X_{eq} = 36.83$ mm.

3.4 Stability Discussion

As mentioned in the previous section, below a certain Re, the spheres developed a circular orbit about a point which is eccentric to the cylinder axis. The critical equilibrium position X_c and Re for the onset were measured,

defining as the critical point the Reynolds number, Re_c, where the standard deviation of the position of the sphere was bigger than 5% the radius of the sphere and X_c the correspondent equilibrium position. In figure 3.4 a plot of X_c as a function of the size of the sphere is shown.

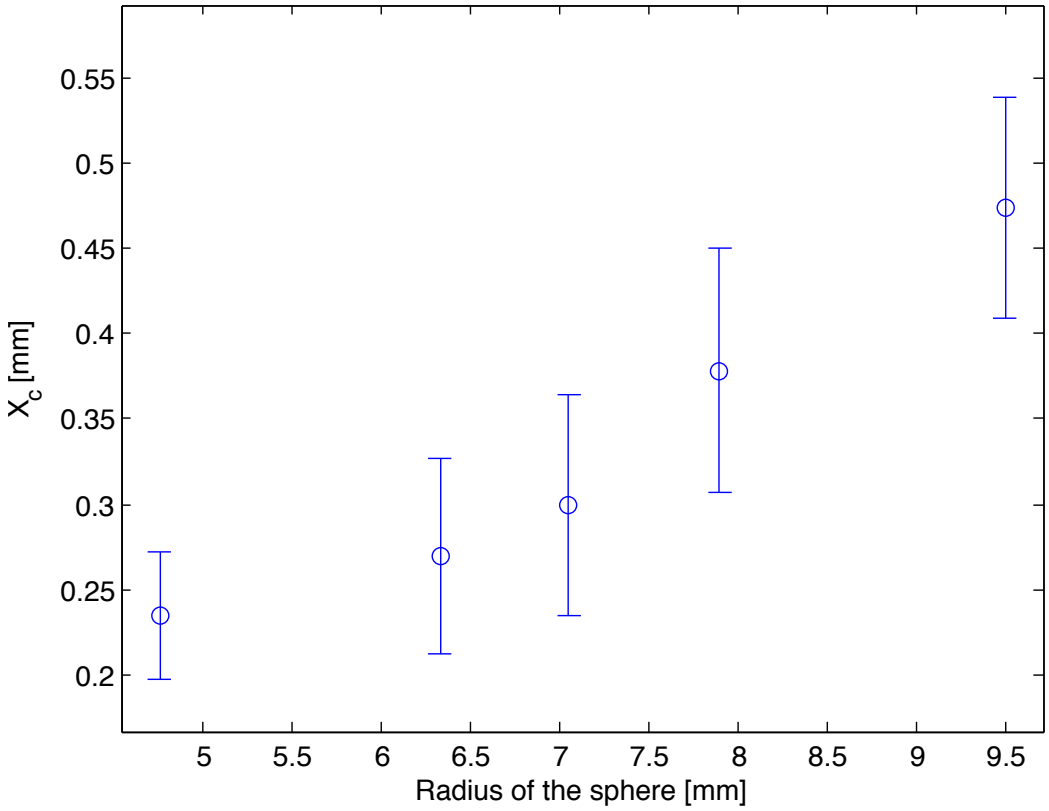

Figure 3.4: Critical equilibrium position plotted against the radius of the sphere; the stability range of the fixed point behaviour depends on the size of the sphere

Here it can be seen that the eccentric fixed point range is bigger for larger spheres and smaller for smaller spheres. This result connects the predictions of the model presented here with the Stokesian calculations of Lee and Ladd [36] for a point like particle. In the calculations made by Lee and Ladd the

only predicted fixed point is in the centre of the cylinder. If the stability range of the fixed points grows monotonically with the size of the sphere, then it suggest that for an infinitely small sphere, one could only expect a single fixed point at the centre of the cylinder.

3.5 Summary

The results in this chapter show that, as predicted by the model, the spheres have a range of stable fixed points for all the sizes of spheres presented here. The experimental result also indicate that the fixed points become unstable below a certain critical Reynolds Re_c.

The experimental results show a remarkable agreement with the presented model, shedding a light in which are the relevant forces that describe this system; a viscous drag F_D ,a centripetal force F_C and the buoyancy force F_B. This forces are enough to describe the eccentric equilibrium position and the centre of the oscillations after the sphere becomes unstable.

It was also found that the stability range of the fixed points depends on the size of the spheres when its density is kept constant. Our results suggest that the stability range grows monotonically to the size of the sphere. Connecting the existent Stokesian calculations, for a point like particle and infinitely small Reynolds number, where an off centre equilibrium position is not found.

The next chapter moves on to discuss the circular orbits mentioned in this chapter in further detail.

Chapter 4

Orbits

In this chapter, the experimental results regarding the regime in which the sphere orbits about a fixed point are presented. In section §4.1 the trajectories of a sphere which describes circular orbits are discussed. Circular orbits were found when decreasing the Reynolds number below the values at which the eccentric fixed points presented in chapter 3 were found.

The growth rate of the oscillations and their onset are discussed in section §4.1.1. In section §4.2 the ratio between the angular velocity of the sphere and that of the cylinder is shown.

In section §4.3 the results of an investigation into the development of oscillations from fixed points close to the cylinder walls are presented. These oscillations appeared when the Reynolds number was increased to $Re \approx 0.01$. Below $Re \approx 0.01$ the sphere sat at a stable fixed point adjacent to the cylinder wall. The fixed point was located at approximately the mid-plane of the cylinder. The onset of the oscillations by the wall, are compared with those found for the onset of oscillatory motion in the centre of the cylinder in section §4.1.

4.1 Circular Orbits

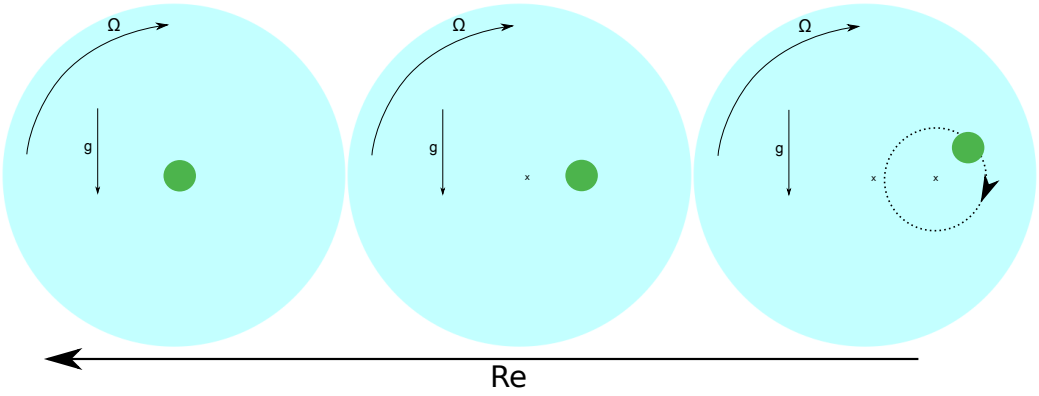

Figure 4.1: Schematic diagram of the dynamical regimes under study. Re decreases from left to right. At the left, the sphere sits in the centre of the cylinder. In the middle the sphere settles at an off-centre fixed point. At the right, the sphere describes circular orbits about the original fixed point

As mentioned in the previous chapter, below a critical Reynolds number Re_c the sphere began to move in a limit cycle, with the form of circular orbits about its eccentric equilibrium position as shown in figure 4.1

To study these orbits, the position of the sphere was measured using the fast camera. Image sequences were acquired at a rate of 50 fps and each sequence comprised 500 frames. This was the maximum amount of frames our camera could record considering the size of the images needed to capture the entire range of movement.

The position of the centre of the sphere was measured for each image in the sequence, so the trajectory of the sphere tracked over time. This is shown in section a) of figure 4.2. Here, it can be seen the orbit described by a sphere of radius $a = 7.9$ mm when $Re = 0.298$. The circles correspond to the the position of the centre of the sphere, and the centre of the orbit is marked with

a black x. The solid line represents a circular fit to the experimental data obtained by least square minimisation. The radius of the orbit was obtained from the fit.

In section b) of figure 4.2 several orbits are shown. Each orbit was obtained for a different Reynolds number.

Considering that the Reynolds number is such that $0.1 < Re < 2$, the smallest orbits, correspond to the dynamical motion of the sphere at higher Reynolds numbers. The centre of these orbits is closer to the central axis of the cylinder. The bigger orbits, on the other hand, correspond to motion at low Reynolds numbers. The centres of these orbits are further away from the central axis of the cylinder and closer to the cylinder wall, getting as close as 2 cm from the wall without losing circularity. In other words, for decreasing Reynolds number both the orbital radius and the distance between the central axis of the cylinder and the orbital centre increase.

The average position of the centre of the sphere, presented in the previous chapter, coincides with the centre of the orbit because this limit cycle is circular. Looking back to figure 3.3 in the previous chapter, where the average position of the sphere is plotted as a function of the Reynolds number, the data points with relatively large error bars, depicting a large standard deviation from the average position, corresponded to spheres in this oscillatory regime. Moreover, the prediction of the equilibrium position, by the model presented in the previous chapter [44], predicts the position of the fixed points, and also coincides with the position of the centre of the orbits after the fixed points have became unstable.

In figure 4.2 it can also be seen that there is a range of Reynolds numbers where the size of the orbit is very small, less than 5% the radius of the

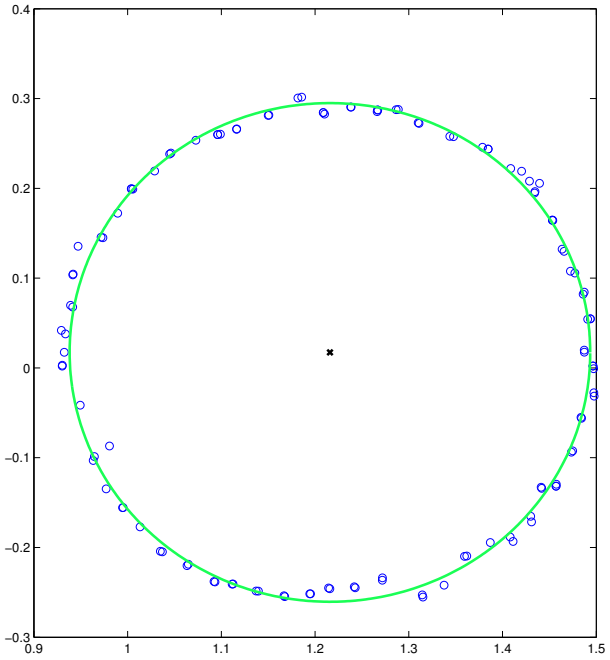

(a)

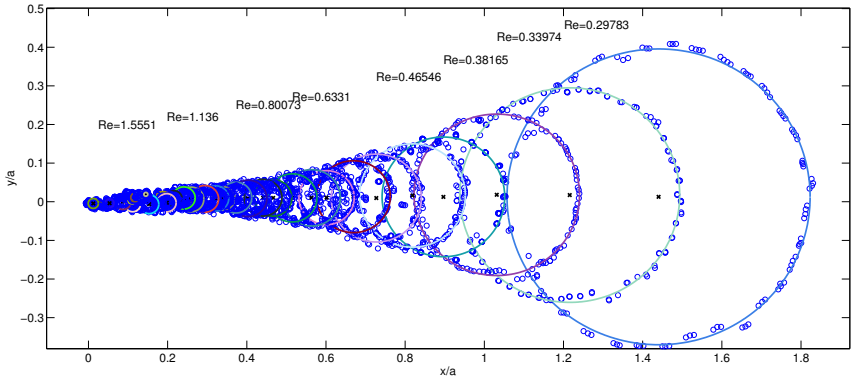

(b)

Figure 4.2: a) Orbit described by a sphere of radius $a = 7.9$ mm at Reynolds number $Re = 0.298$ b) Orbits for a sphere of $a = 7.9$ mm of radius. Each trajectory corresponds to a fixed Reynolds number. The radius of the orbit grows bigger when decreasing the Reynolds number

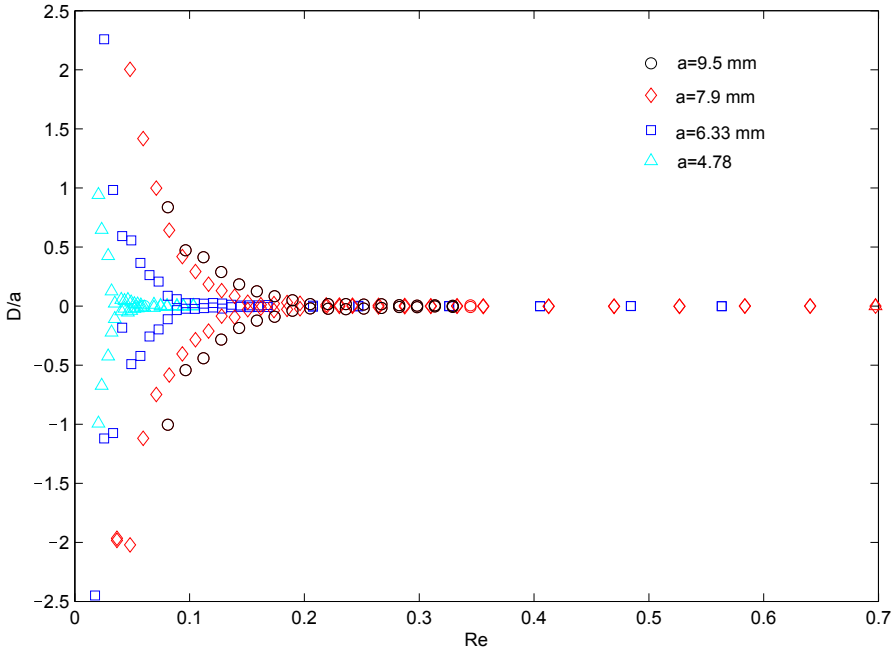

Figure 4.3: The maximum vertical displacement D of a sphere nondimensionalized by the sphere radius a is plotted as a function of Re for spheres of different radius. $\triangle$ corresponds to $a = 4.78$ mm, the $\square$ corresponds to $a = 6.33$ mm, the $\Diamond$ to $a = 7.9$ mm and $\bigcirc$ to $a = 9.5$ mm

sphere. This is because in this range, $Re > 0.2$ the sphere is actually in a fixed point. This can be observed better in figure 4.3. Here, the maximum vertical displacement of the sphere nondimentionalized by the corresponding radius of the sphere is plotted as a function of the Reynolds number. It can be seen that the oscillations occur at smaller Reynolds numbers, for smaller spheres and at higher Reynolds numbers for bigger spheres.

4.1.1 Growth rate of the orbital radius

The dependence of the radius of the orbit described by the sphere as a function of the Reynolds number was investigated for all the spheres in this study.

As mentioned in the previous section, a circle was fitted to the trajectory using a least square method, resulting in the coloured solid lines shown in figure 4.2. In this way the radius of the orbit was found as a function of the Reynolds number as shown in figure 4.4, the error bars here indicate the mean squared error in the fit of the orbit.

An interesting aspect of section (a) of figure 4.4, is that the growth of the orbital radius seems to grow slowly when $Re > 0.2$ and very fast at the when $Re < 0.2$. and does not seem to saturate for the orbits considered here, which were away from the walls of the cylinder.

To look in more detail to the growth rate of these orbits in figure 4.5 the case of the sphere of radius $a = 7.9$ is looked closely.

Observing section a) of figure 4.5, it can be seen that a linear function can be adjusted to the radius of the orbit as a function the Reynolds number in logarithmic scale. When doing so it was found that the slope of this line was very close to 2.

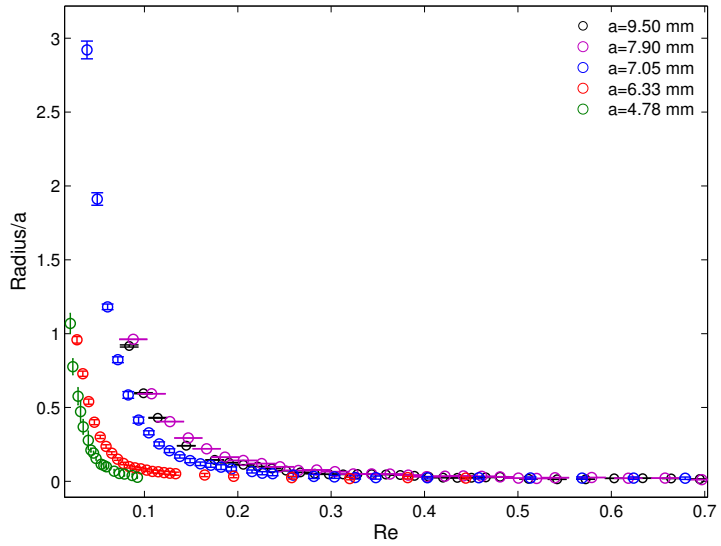

(a)

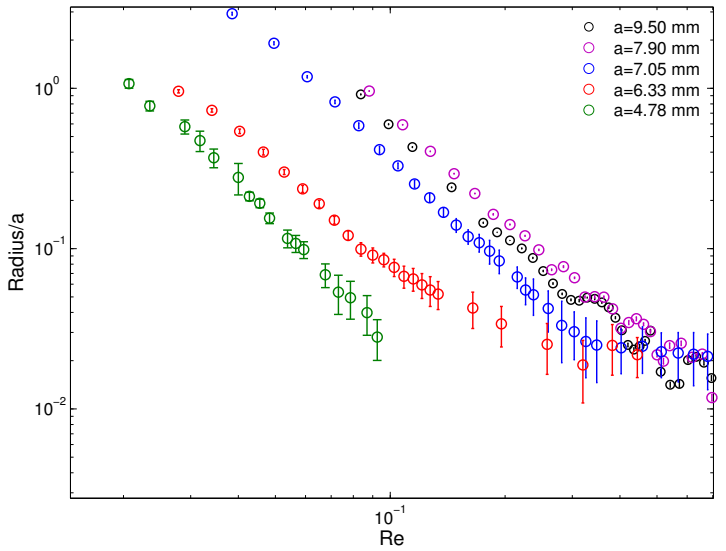

(b)

Figure 4.4: Radius of the orbits in function of the Reynolds number for spheres of different radii. The green data corresponds to a sphere of radius $a = 4.78$ mm the red data to $a = 6.33$ mm the blue data to $a = 7.05$ mm the black data to $a = 7.9$ mm and the magenta data to $a = 9.5$ mm. Section (a) shows it in linear scale while section (b) in logarithmic scale.

Furthermore, if looking at the radius of the orbit as a function of the Reynolds number for a sphere of $a = 7.9$ mm in section b) of figure 4.5 it can be observed that the best fit to this data corresponds to:

$$R(Re) = \frac{c_1}{Re^2} + c_2, \tag{4.1}$$

where R corresponds to the orbital radius, $c_1 = 0.01751 \pm 0.0008$ and $c_2 = -0.032 \pm 0.0102$. The parameter describing this bifurcation is $\varepsilon = \frac{1}{Re}$. The constant c_2 was included in the fit to take into account the noise in the system.

This growth rate does not correspond to a Hopf bifurcation, where the growth rate is expected to be $\sqrt{\varepsilon - \varepsilon_0}$.

It was also checked, that there was no hysteresis for this transition. To do so, the orbital radius was measured for a sphere of radius $a = 7.05$ mm. The Reynolds number was first decreased from $Re \approx 2$ to $Re \approx 0.1$ in small steps and a measurement was taken for each step. Then the Reynolds number was increased from $Re \approx 0.1$ in small steps taking measurements for each steps.

The result of this measurement are shown in figure 4.6, where it can be seen there is no hysteresis in the system.

4.2 Frequency of rotation

The frequency of rotation of all the spheres used in this study, was measured as a function of the Reynolds number.

This measurement was obtained by tracking the orientation of markings on the sphere throughout a complete rotation cycle. For each sphere, 10 cycles were measured for each Reynolds number.

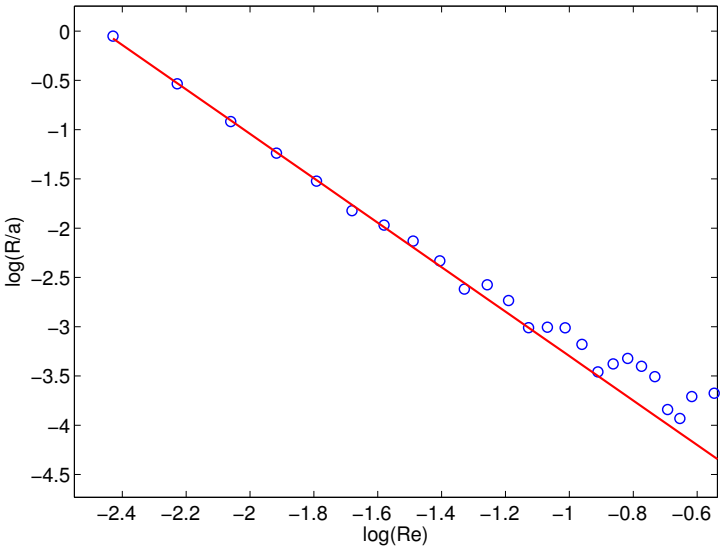

a)

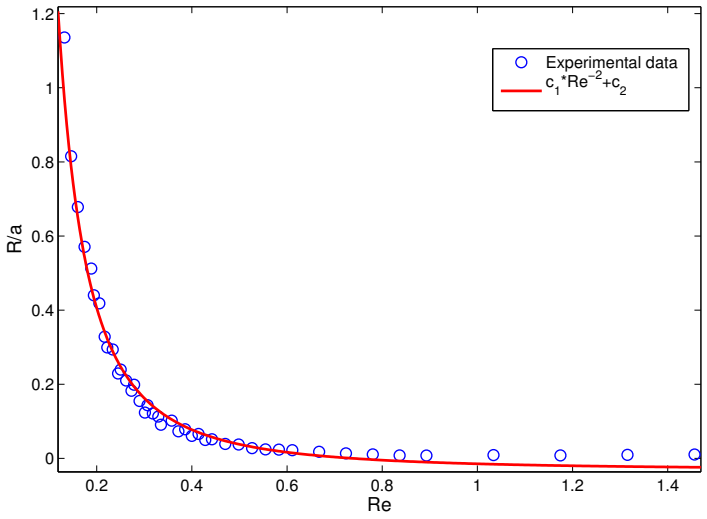

b)

Figure 4.5: a) Orbital radius as a function of the Reynolds number in logarithmic scale and a linear fit of slope 2 for the sphere of radius a=7.9 mm. b)Orbital radius for a sphere off $a = 7.9$ mm of radius and a fit of the form $R(Re) = c_1 Re^{-2} + c_2$ with $c_1 = 0.01751 \pm 0.0008$ and $c_2 = -0.032 \pm 0.0102$.

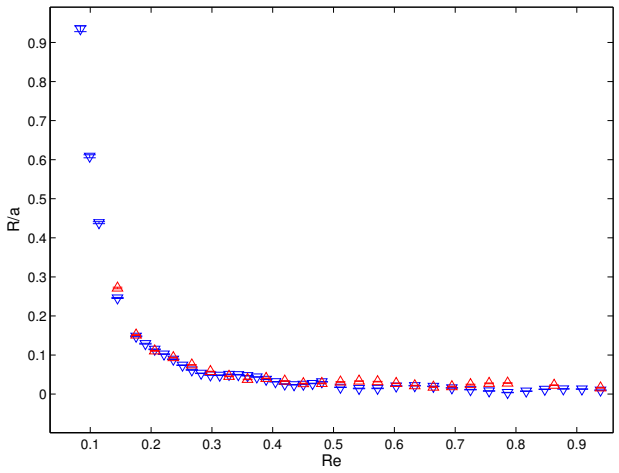

Figure 4.6: Orbital radius for a sphere of radius $a = 7.05$ mm, the orbital radius was measured increasing $\triangle$ and decreasing $\triangledown$ the Reynolds number, no hysteresis was observed

The results of this measurements are shown in figure 4.7, here the data points represent the ratio between the rotation speed of the sphere and the rotation speed of the cylinder, measured for each Reynolds number. The error bars represent the standard deviation of each measurement. When taking an average value of the ratio between the angular velocity of the spheres and the angular velocity of the cylinder for all spheres a value of 0.88 is obtained.

Given that the value of the ratio between the angular velocity of the spheres and the cylinder is relatively close to 1 ($\omega/\Omega = 0.88$), it was necessary to ensure that the oscillations were not forced by some perturbation in the apparatus.

Hence, a periodic perturbation was introduced by glueing a small cylinder of 3 mm of radius and 180 mm of length, lengthwise in the inner wall of the rotating cylinder, which created a periodic radial disturbance to the flow.

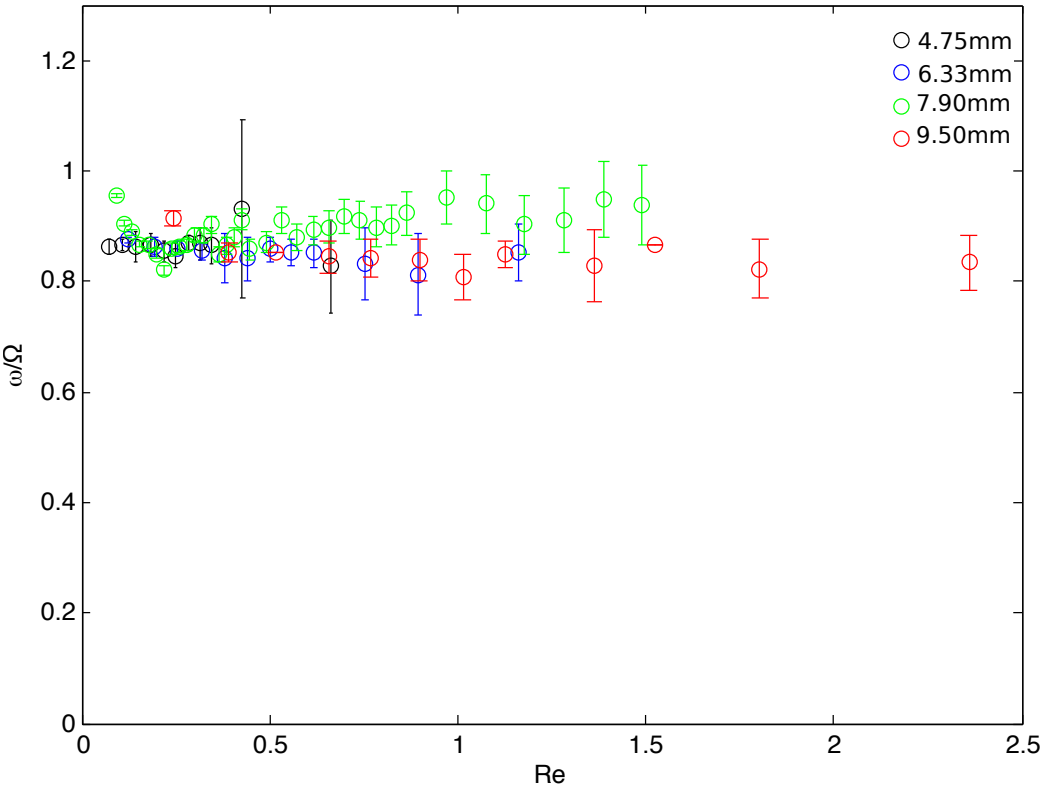

Figure 4.7: Ratio between the frequency of rotation of the sphere and the frequency of rotation of the cylinder ω/Ω as a function of the Reynolds number. The average value of the rotation rate of the spheres over the rotation rate of the cylinder is 0.88, indicating the oscillations are not an artefact of the rotation of the cylinder

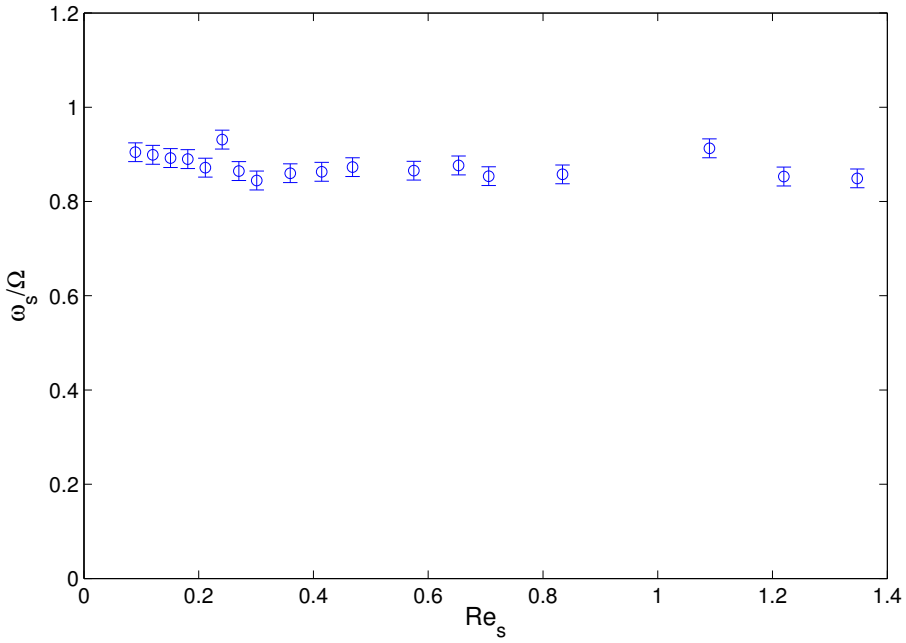

Figure 4.8: Ratio between the frequency of rotation of the sphere and the frequency of rotation of the cylinder ω/Ω when a radial obstacle has been placed inside of the cylinder, which does not have a significant effect on the rotation of the sphere of $a = 6.33$ mm.

The ratio between the angular velocity of a sphere of radius $a = 6.33$ mm and the angular velocity of the cylinder was measured in the same fashion as it was measured for the experiment without the perturbation. The results of this measurements are shown in figure 4.8, where the ratio between the angular velocity of the sphere and the angular velocity of the cylinder is plotted against the Reynolds number.

The average value of the ratio, in this case was 0.875, from which it can be concluded that a perturbation of this size does not have a significant effect on the rotation of the sphere.

4.3 Oscillations from the wall

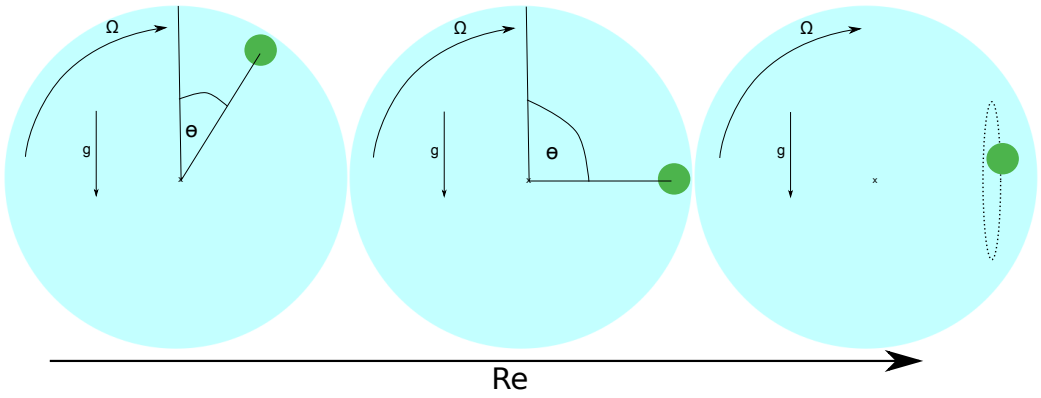

Figure 4.9: Schematics of the onset of the oscillation by the wall; when increasing the Reynolds number, the angle formed between the sphere and the vertical θ grows until it reaches $\theta = 90°$. When the Reynolds number is increased even more, the sphere starts oscillating vertically

As discussed above and in the work of Mullin [23] and in detail in the thesis of Otto [53], for a negatively buoyant sphere, when the cylinder is

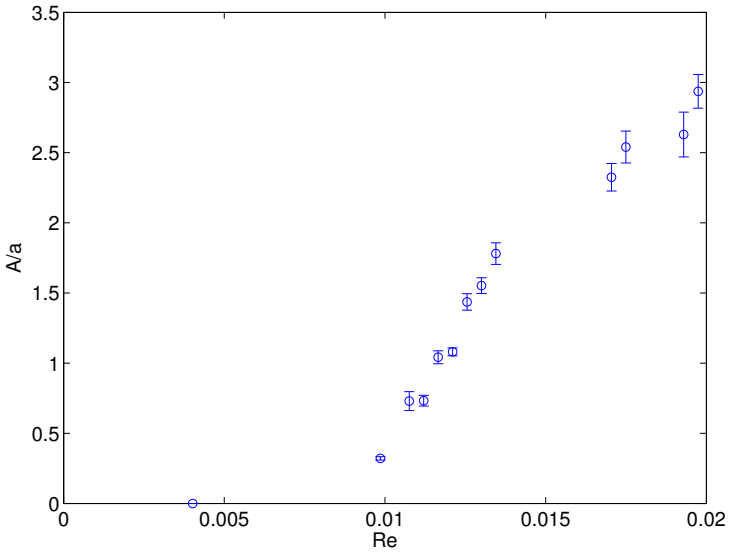

Figure 4.10: Amplitude of the oscillations from the wall for a sphere of radius $a = 7.9$ mm

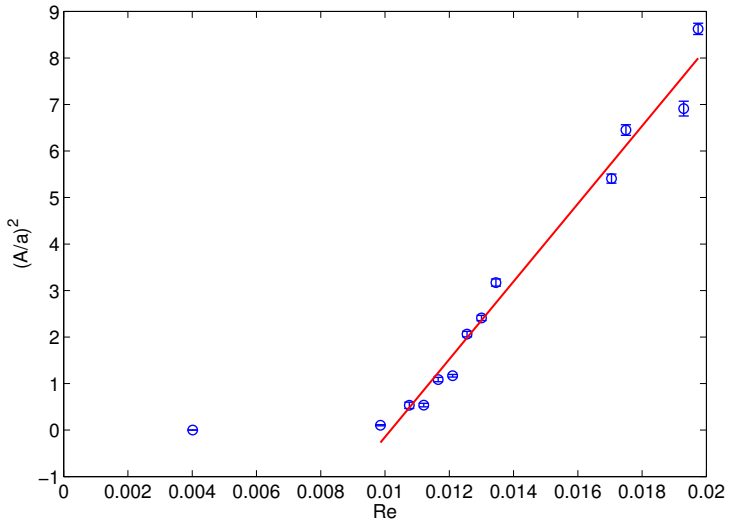

Figure 4.11: Square of the amplitude of the oscillations from the wall for a sphere of radius $a = 7.9$ mm, a linear fit of the form $p_1 Re + p_2$, with $p_1 = 835.8$ and $p_2 = -8.508$, is shown in a solid line.

rotating at very low speed, the sphere will stay at a fixed point by the wall. This fixed point can be described by the angle θ formed between the vertical and the sphere. The angle θ increases when increasing the Reynolds number until reaching $\theta = 90°$ at a critical Re_{wall}, position at which the sphere detaches from the wall and oscillated vertically as shown in figure 4.9 .

The onset of near wall oscillations was investigated for a sphere of $a = 7.9$ mm. The amplitude of this oscillations in the vertical direction was measured and plotted as a function of the Reynolds number, this is shown in figure 4.10

It can be seen in figure 4.11 that the square of the amplitude has a growth which is linear in the Reynolds number, which means the amplitude of this oscillations grow as as the square root of the Reynolds number. A linear fit of the form $p_1 Re + p_2$, with $p_1 = 835.8$ and $p_2 = -8.508$ is shown in the figure. The critical $Re_{wall} = 0.0102$ can be obtained from the fit. The square root dependance from the bifurcation parameter, plus the periodicity of this orbits indicates that these near wall oscillations have the shape of a Hopf bifurcation, which is in agreement with the results obtained by Otto [53] for a heavy sphere.

This is particularly interesting considering that the onset of the oscillations that grow from the fixed point have an atypical growth rate of $\frac{1}{Re^2}$ which these oscillations do not have. This suggests there must be a feedback mechanism in the oscillations from the fixed point given by the sphere being free to move and feeling the wake that leaves behind its own orbit.

4.4 Summary

The experimental results described in this chapter show that the first instability of the fixed point described in the previous chapter corresponds to a simple periodic motion, the sphere describes a circular orbit centred at the original fixed point.

It has also been shown that the growth rate of this limit cycle has an unusual growth rate that suggests the presence of a feedback mechanism in the orbits that grow from the fixed points. Considering that the sphere is free to move, this might be given by a resonance between the sphere and the wake which is left behind the sphere.

We have shown that the oscillations are not a result of resonances in the system and that a periodic perturbation does not have a significant effect in the rotation of the sphere.

It has also been shown that when the Reynolds number is increased from zero up to $Re = 0.01$ the sphere stays at a fixed point by the wall of the cylinder. Over that value of Re, this fixed point became unstable and the sphere oscillated vertically.

These near wall oscillations, when increasing the Reynolds number, do grow as a Hopf bifurcation, because there is a square root dependance between the amplitude of the oscillation and the Reynolds number. This coincides with the kind of bifurcation reported previously by Mullin [23] and Otto [53] for a heavy sphere oscillating near the wall of a rotating cylinder.

Chapter 5

A Porous Sphere

A porous sphere was fabricated using a 3D printer. The density of the plastic used by the 3D printer was $\rho_{plastic} = 1.17$ g/cm^3 and the sphere had a radius $a = 8$ mm. The sphere had a typical pore size of 2 mm of diameter and the inside of the sphere was hollow, such that it became completely filled with fluid once the sphere was immersed in glycerol. The effective density of the porous sphere was calculated using the the mass of the sphere when dry to calculate the volume fraction filled with plastic and the fraction filled the glycerol. The effective density was estimated to be $\rho_{porous} = 1.244$

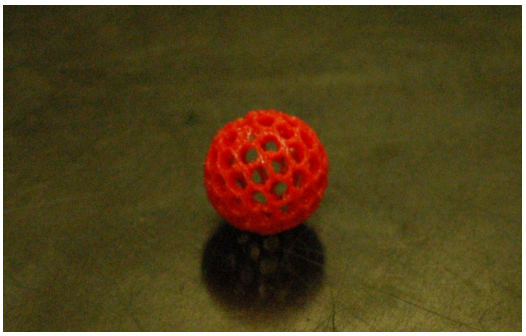

Figure 5.1: A porous sphere fabricated in a 3D printer of radius $a = 8$

The properties of this sphere, resemble those of a biological scaffold which allows the exchange of nutrients from the culture media, so it needs to be porous. Also, to minimise shear and disturbances, the terminal velocity is minimised by choosing scaffold and culture media with similar densities [22]. In this case, the density ratio was $\rho_{porous}/\rho_{glycerol} = 0.9873$.

In section §5.1 the average position of the porous sphere is presented as a function of the Reynolds number. This position is compared with the theoretical predictions for a solid sphere with the terminal velocity of the porous sphere which was determined experimentally. The average position of the porous sphere is also compared with the average position obtained previously for a solid polypropylene sphere of radius $a = 7.9$ mm, which was the most similar available sphere in this investigation.

Below a critical Reynolds number, the porous sphere starts describing circular orbits about the average position presented in section §5.1 In section §5.2 the radii of this orbits, are presented. This radius is compared with the previously obtained radius of the orbits described by a solid sphere of radius $a = 7.9$ mm.

In section §5.3 the onset of the oscillations by the wall is presented. As for a solid sphere, this happened when increasing the Reynolds number from very small values. When $Re \approx 0.005$ the sphere remains at a fixed point by the wall described by the angle θ that the sphere forms with the vertical, θ increases when increasing the Reynolds number until $Re \approx 0.01$ when $\theta = 90°$ when the sphere became unstable and starting oscillating vertically.

5.1 Average postion

The averaged position of a porous sphere of a radius of $a = 8$ mm was measured as a function of the Reynolds number. The measurements were made following the procedure outlined in chapter 3 for the solid spheres. In this case, image sequences of 120 frames were recorded at a frame rate of 20 frames per second. A time of at least 2 minutes was allowed between two measurements to ensure that the fluid was rotating at solid body rotation after changing the frequency of rotation. This time is much bigger than the viscous diffusion time (3.2 sec) and the spin up time (1.8 sec) defined in chapter 3.

In figure 5.2 the averaged position of the porous sphere is plotted as a function of the Reynolds number. To compare, the averaged position of a solid, polypropylene sphere of radius $a = 7.9$ mm is also shown in this figure. The error bars in this figure correspond to the standard deviation of the position of the centre of the sphere over an image sequence, acquired for at a specific Reynolds number. The most relevant feature that can be seen in this plot is that the porous sphere remained much closer to the central axis of the cylinder over the entire range of Reynolds numbers, while the solid sphere goes to an eccentric equilibrium position. For $Re < 0.3$ the average position moved slightly off centre, less than 10% the radius of the sphere. For $Re < 0.2$ the error bars, representing the standard deviation on the averaged position, increased, as the porous sphere prescribed circular orbits.

In figure 5.3, the averaged position of the porous sphere is shown as a function of the Reynolds number. The solid line represents a theoretical curve obtained using the model presented in chapter 3 [44]. The model assumes

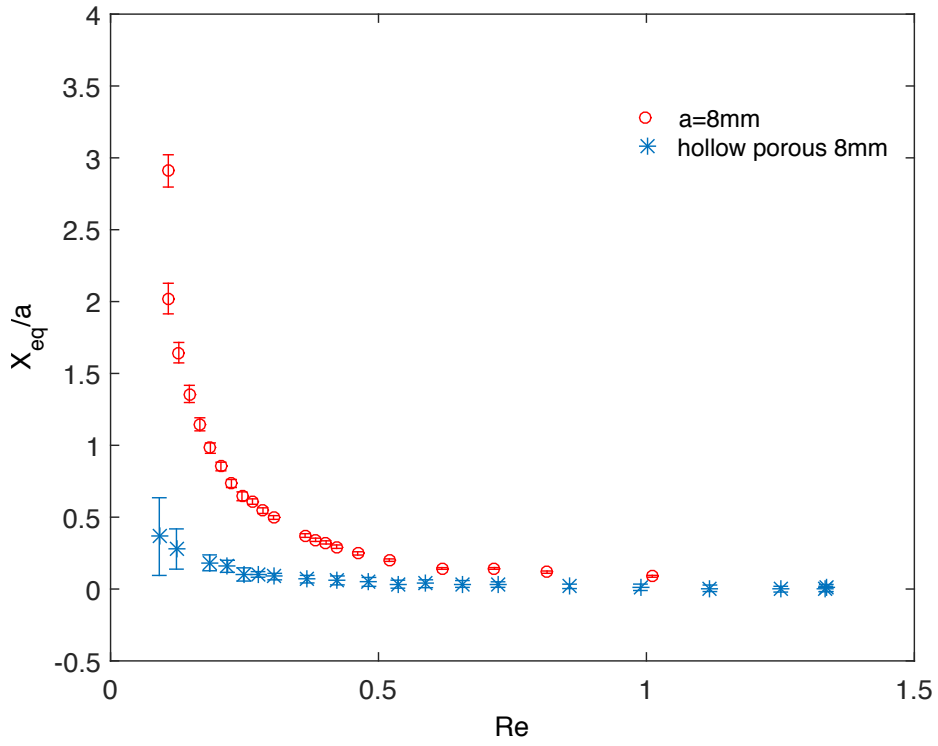

Figure 5.2: The equilibrium position of a porous sphere of radii $a = 8$ mm plotted as a function of Re is shown in $*$. The red circles correspond to the equilibrium position of a smooth solid sphere of a=7.9 mm

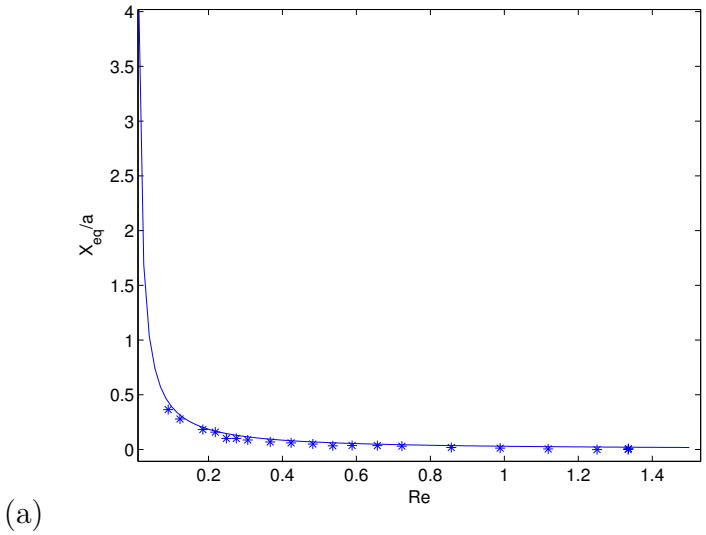

(a)

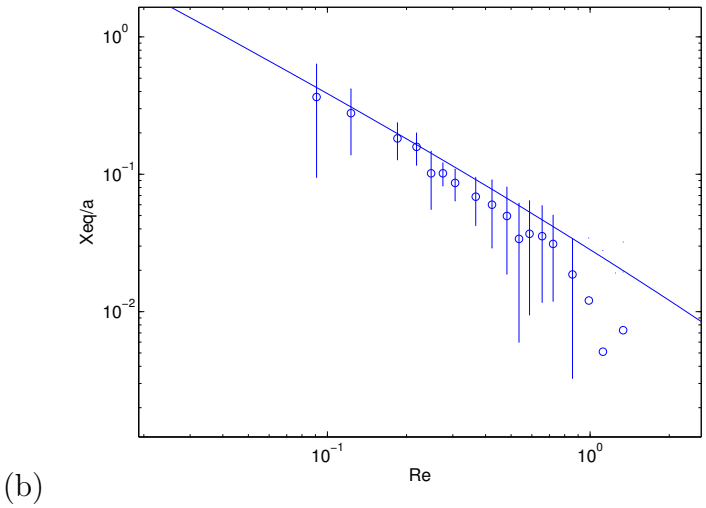

(b)

Figure 5.3: Equilibrium position of a porous sphere of radii $a = 8$ mm as a function of Re, the solid line represents the theoretical equilibrium position predicted by the model (a) shows it in linear scale and (b) in logarthmic scale

a solid sphere and takes into account that the forces acting on the sphere, buoyancy, drag and centripetal, are such that the equilibrium position is as stated in equation 3.9 and it is proportional to Re_p, meaning that x is also proportional to the terminal velocity V_T.

In the case of the porous sphere, the terminal velocity is an order of magnitude smaller than the terminal velocity for a solid sphere ($V_{Tporous} = 0.0062$ m/s while $V_{Tsolid} = 0.0505$ m/s). This results from the pores in the sphere surface which allow glycerol to enter and fill the sphere such it becomes nearly neutrally buoyant, making the terminal velocity much smaller.

It can be seen in figure 5.3 that the agreement between the theoretical model and the experimental data is very good. This suggests that the inclusion of the experimental value of the terminal velocity in the model averages the effects of the porosity on the balance of forces.

5.2 Oscillations of the porous sphere

The porous sphere, as the solid spheres presented in the previous chapter, becomes unstable below a critical Reynolds number and start oscillating. In this case, this happened for Reynolds numbers $Re < 0.25$. The centre of this orbits corresponded to a point which is off centre with respect to the central axis of the cylinder.

In figure 5.4, the radius of the orbit described by the porous sphere is shown. In this figure it can be seen that the onset of the oscillations is delayed in comparison with the solid sphere, the porous sphere remains without oscillating for lower Reynolds numbers.

An expanded view of the data is presented in the insert of figure 5.4. Here it can be observed that the measured radius of the orbit is below 5% of the radius of the sphere for all data points when $Re > 0.25$ which is the criteria used previously to decided that the sphere was on a fixed point.

From this it can be concluded that a porous sphere is more stable than the

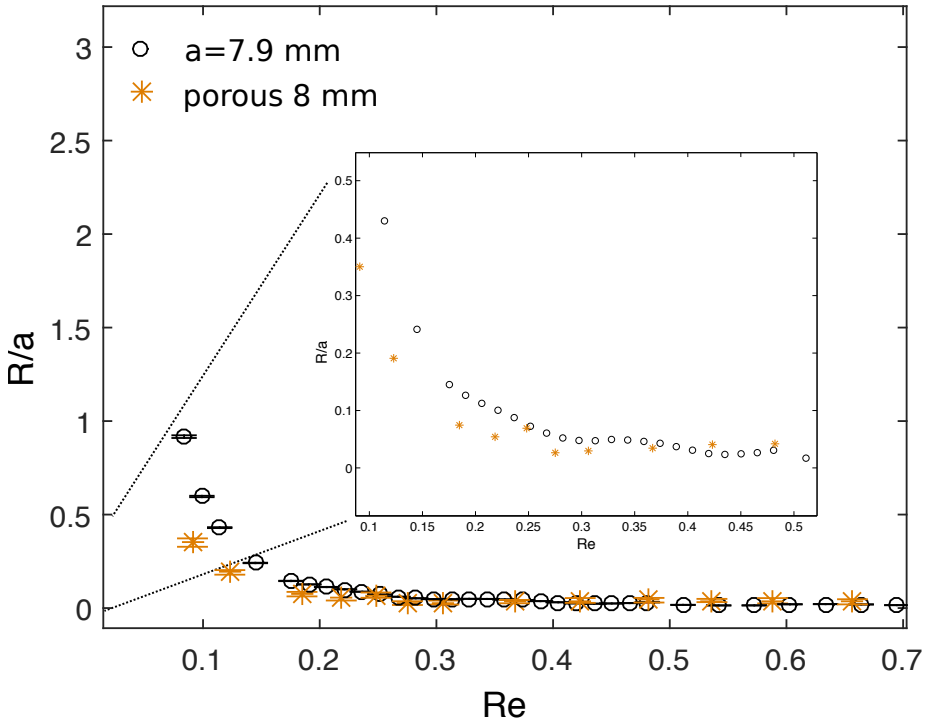

Figure 5.4: Radius of the orbit described by a porous sphere of radii $a = 8$ mm compared with the radius of the orbit described by a smooth solid sphere of a=7.9 mm as a function of Re. A zoom to the data set for the porous sphere is also shown, from here it can be seen that when $Re > 0.2$, the measured radius of the orbit, is below 5% the radius of the sphere.

a solid sphere of similar radius. The porous sphere actually, does not oscillate for $Re > 0.25$ while the solid sphere of the same size becomes unstable for $Re < 0.3$.

5.3 Oscillations from the wall

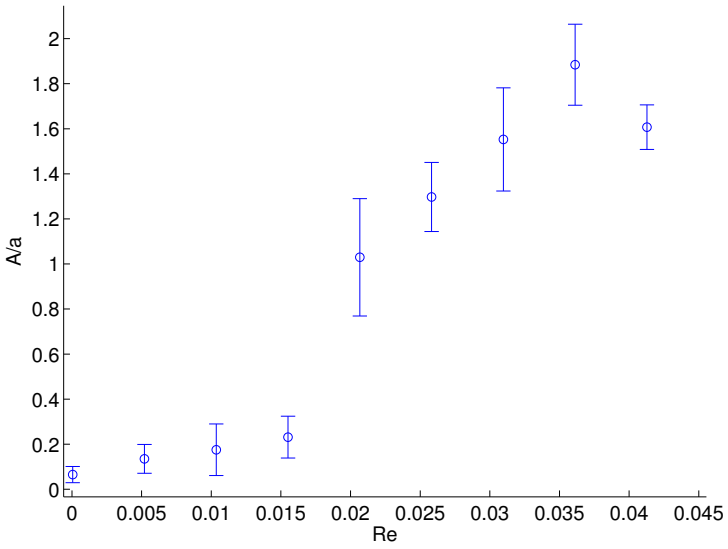

Figure 5.5: Amplitude of the oscillation described by a porous sphere of radii $a = 8$ mm by the wall, plotted as a function of Re.

As described in chapter 4, a positively buoyant sphere finds equilibrium positions by the wall of the rotating cylinder when this is rotating at very low speeds. This position can be described by the angle θ that the sphere forms with the vertical. The onset of the oscillations occurred when this angle is $\theta = 90°$ and the sphere detached from the wall. The sphere then oscillated in the vertical direction.

In figure 5.5 the amplitude of this oscillations is shown as a function

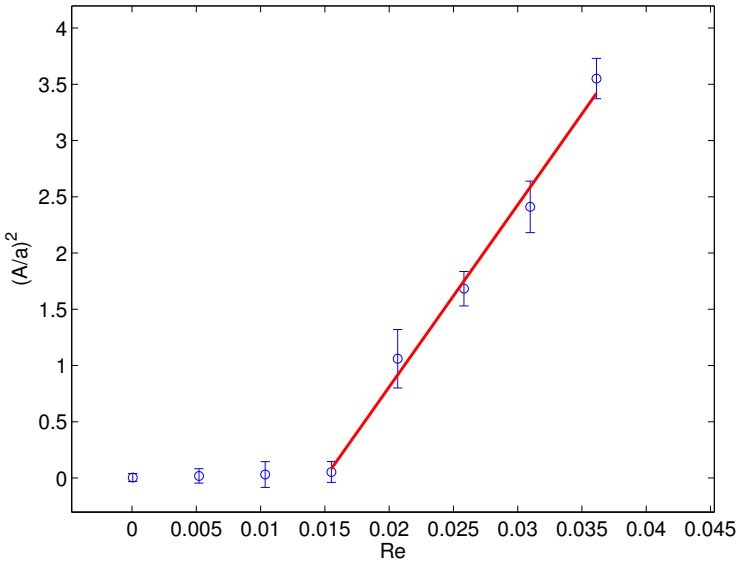

Figure 5.6: Square of the amplitude of the oscillation described by a porous sphere of radii $a = 8$ mm by the wall plotted as a function of Re. The red solid line corresponds to a linear fit of the form $p_1 Re + p_2$, with $p_1 = 161.9$ and $p_2 = -2429$, is shown in a solid line

of the Reynolds number. This plot suggest the amplitude goes through an imperfect pitchfork bifurcation, but the square root dependence on Re needs to be confirmed. To do so, a plot of the square of the amplitude as a function of Re is shown in figure 5.6. In this plot, a linear fit of the form $p_1 Re + p_2$, with $p_1 = 161.9$ and $p_2 = -2429$ has been added to the data that was away from zero, confirming that the amplitude have a square root dependance on the Re. The critical Re at which the oscillation starts is $Re_{wall} = 0.0150$ which was obtained from the fit.

An interesting aspect is that, as for the solid spheres, the onset of the oscillations from the wall have a different dynamics than that of the onset of the circular orbits.

5.4 Summary

From the results presented in this chapter, it is possible to make three major observations regarding the behaviour of a porous sphere in comparison with a solid sphere of similar size.

The first one, is that even though an eccentric equilibrium position exists for a porous sphere, this fixed point is closer to the central axis of the cylinder and experimentally is much more difficult to detect than for a solid sphere. Nevertheless, the model [44] still predicts the position of the porous sphere, if the terminal velocity to be considered for this sphere, is the one that has been measured experimentally and presented in chapter 2. This is despite the fact that the model assumes the sphere is solid, because the measurement of the terminal velocity contains information about the balance between the drag and the buoyancy forces acting on the sphere.

The second is that the porous sphere also describes circular orbits about a point off the central axis of the cylinder, and this point is still predicted by the model. In comparison with a solid sphere of similar size, the porous sphere has a larger stability range in terms of Re, meaning it remains without oscillating for lower Reynolds numbers than the solid sphere.

The third one, is that the behaviour of the porous sphere when oscillating by the wall is qualitatively similar to the onset of the oscillations for the solid sphere. The onset of the oscillations occurred at a similar Reynolds number $Re = 0.01$. The difference here, was the coefficient of the amplitude of this oscillations, that in the case of the porous sphere was much smaller.

Regarding the dynamic of a biological scaffold, this results suggest that a smaller terminal velocity can have a stabilising effect, increasing the Reynolds number range at which tissue can be grown inside of a rotating bioreactor, avoiding the onset of oscillations. It is also important to notice that porosity is necesary for biological scaffolds, otherwise the exchange of nutrients would not be possible.

Chapter 6

Rough Spheres

The results of an investigation into the effects of roughness on the motion of the spheres are presented in this chapter. Spheres with three different roughness were made in the 3D printer using ABSplus plastic. The roughness was created by fabricating spheres of 6 mm of radius with 10 small hemispherical bumps uniformly distributed in the surface such that the resulting roughened spheres had outer radii $a_{max} = 8$, 7.5 and 7 mm respectively and inner radius $a_{min} = 6$ mm. An average radius was defined for the three spheres calculated as $a_{mean} = (a_{max} + a_{min}/2)$These spheres can be seen in figure 6.1.

A control sphere of radius $a = 7$ mm was also made in the 3D printer, to compare the data obtained for the rough spheres against a sphere equal same density with a smooth surface. This size of sphere was chosen because it matched the average radius of a sphere with the largest roughness.

Measurements of the average position for spheres of different roughness are reported in section §6.1.

Experimental measurements of the orbital radius described by the rough spheres are shown in section §6.2.

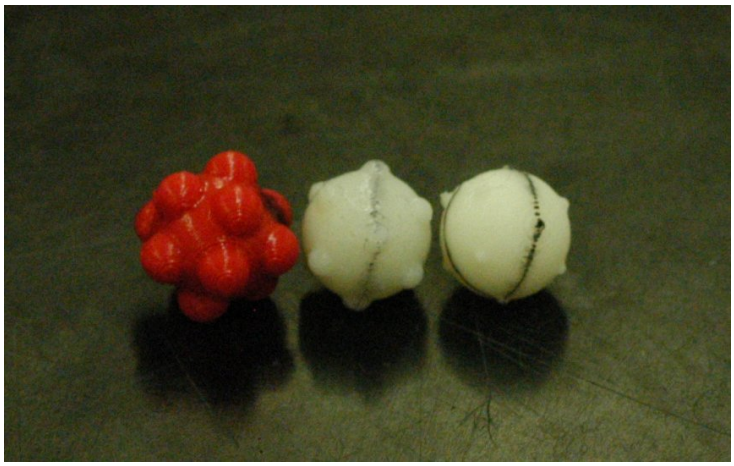

Figure 6.1: A picture of the three rough spheres used for this investigation. All the spheres have an inner radius of $a_{min} = 6$ mm and outer radius of $a_{max} = 8$, 7.5 and 7 mm respectively

6.1 Average Position and fixed points

The average position, measured from the central axis of the cylinder, was obtained for spheres of different roughness by using the same procedure described in previous chapters. For the three spheres considered in this study, image sequences of 500 frames were taken at a frame rate of 20 fps.

The rotational speed of the cylinder was set at a high value ($\omega \approx 20$ $Re \approx 2$) and image sequences were recorded after decreasing the rotational velocity by small steps . A suitable time was allowed after decreasing the rotational speed between two measurements, to allow the fluid to settle to solid body rotation at the new speed. This time was selected using the same criteria used for the smooth sphere, described in chapter §2.

The measured average position is shown plotted as a function of the Reynolds number in figure 6.2 for the three spheres with the different roughness under study.

The prediction of the equilibrium position by the model [44] presented in chapter 3 en equation (3.9)

and is depicted with a solid line for the three spheres in figure 6.2.

In figure 6.2a, the average position for a sphere of outer radius $a_{max} = 6.5$ mm is shown in black. For this sphere the terminal velocity was experimentally measured as explained in chapter 2 and had a value of $V_T = 0.0247 \pm 0.00005$ m/s. This value and an average radius of $a = 6.25$ mm was used in equation 3.9 to obtain the solid black line.

The average position for a sphere of outer radius $a = 7.0$ mm is shown in magenta in figure 6.2b. The terminal velocity of this sphere was $V_T = 0.0237 \pm 0.00007$ m/s and the averaged radius was $a_{mean} = 6.5$ mm. This values were used in equation 3.9 to obtain the solid magenta line.

The average position for a sphere of outer radius $a = 8.0$ mm is shown in blue in figure 6.2c. For this sphere the terminal velocity was measured to be $V_T = 0.0230 \pm 0.00001$ m/s and the averaged radius was $a_{mean} = 7.0$ mm. This values were used in 3.9 to construct the solid blue line.

It can be observed in figure 6.2 that all the spheres settle at an equilibrium position away from the central axis of the cylinder in a qualitatively similar manner as a smooth sphere does.

In all three sections of figure 6.2 the error bars correspond to the standard deviation from the average position. When the size of the error bars increases, for $Re \leq 0.4$, the fixed point becomes unstable and the sphere begins to move in periodic orbits which are centred on the fixed point. The average position in this cases corresponds to the centre of the orbits. The orbits will be described in more detail in the next section.

As expected, the fit of the model [44] is poor for the rough spheres shown

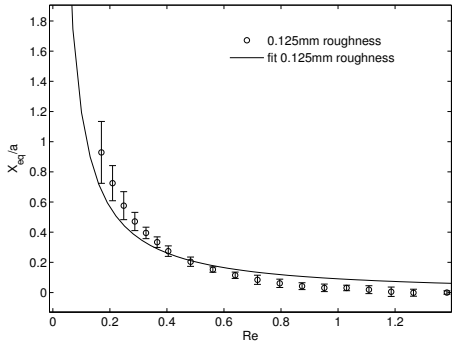

(a) 0.125 mm of roughness

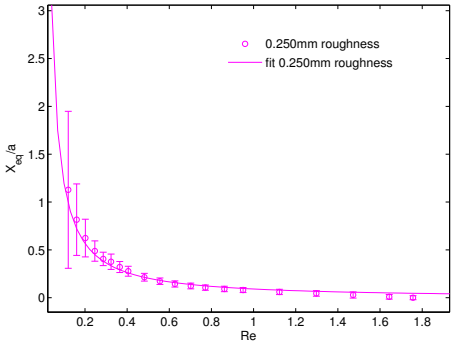

(b) 0.25 mm of roughness

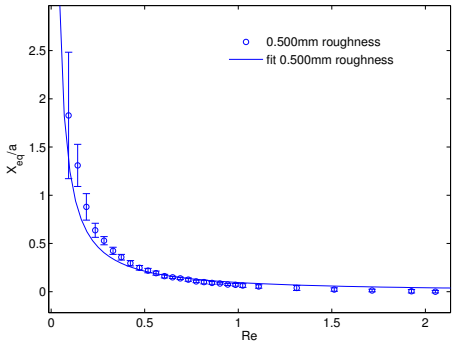

(c) 0.5 mm of roughness

Figure 6.2: Average position as a function of the Reynolds number for spheres of inner radius $a_{min} = 6$ mm and different roughness. In (a) the average position for a sphere of outer radius $a_{max} = 6.5$ mm is shown. In (b) the average position for a sphere of outer radius $a_{max} = 7$ mm is shown. In (c) the average position for a sphere of outer radius $a_{max} = 8$ mm is shown. In all cases the solid line correspond to the prediction of the model. In each the terminal velocity measured experimentally was used to determine the position of the fixed point.

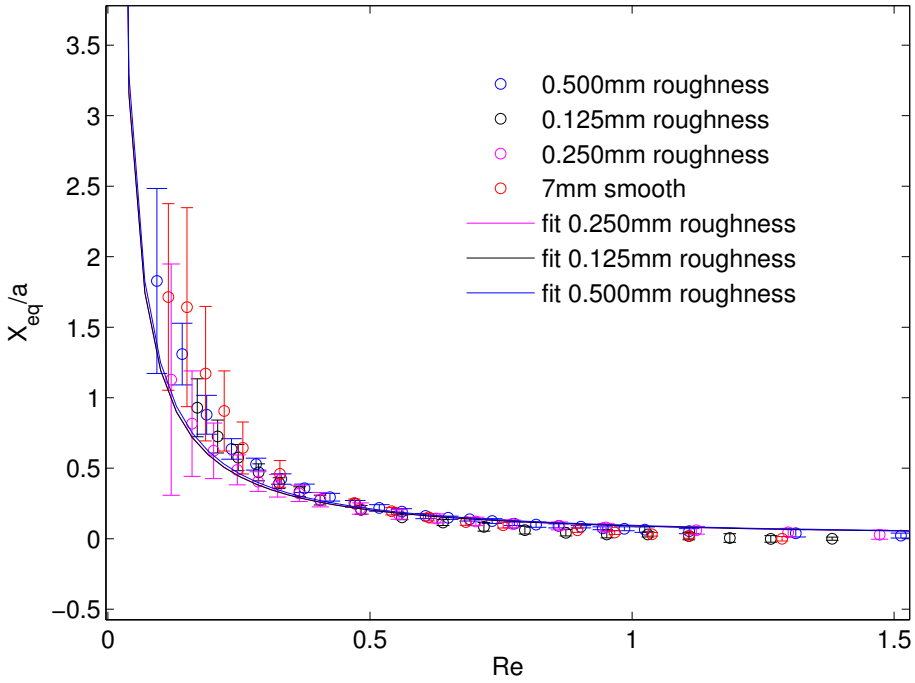

Figure 6.3: Average position of all the rough spheres in this study as a function of the Reynolds number with the prediction given by the model to each one of them, the red circles correspond to the average position of a 3D printed smooth sphere of radius $a = 7$ mm.

in figure 6.3, especially in comparison with how well it fits the data obtained previously for smooth spheres. There are now several important new factors involved. Firstly, the model was developed for smooth spheres and the roughness involved in this experiments are 4.%, 7.7% and 14.3% of the average radius of each sphere. Secondly, the measurement of the terminal velocity was not sensitive enough to establish a clear difference between the different spheres. Third and last, the radius considered here to construct the theoretical curves was the average between a_{min} and a_{max}. This is not necessarily the best way to take into account the size of a rough particle.

In figure 6.3 the averaged position for all the spheres is plotted together with the experimental data for a smooth sphere of $a = 7$ mm is shown in red. It can be seen that there is no significant difference in the average position of the rough spheres compared with a smooth sphere of the same density.

These experimental results indicate that the fixed point behaviour is not affected by the presence of added roughness on the surface of the sphere and is robust to this kind of deviation from sphericity.

6.2 Orbits of the rough spheres

As mentioned previously, the fixed point of the rough spheres also became unstable below a critical Reynolds number. The spheres would then go into a limit cycle, shaped as a periodic circular orbit about a centre displaced from the central axis of the cylinder.

The radius of the orbit was measured following the same procedure described in chapter 4, a circle was fitted to the position of the sphere over a time sequence, and the radius of the orbit was given by this fit.

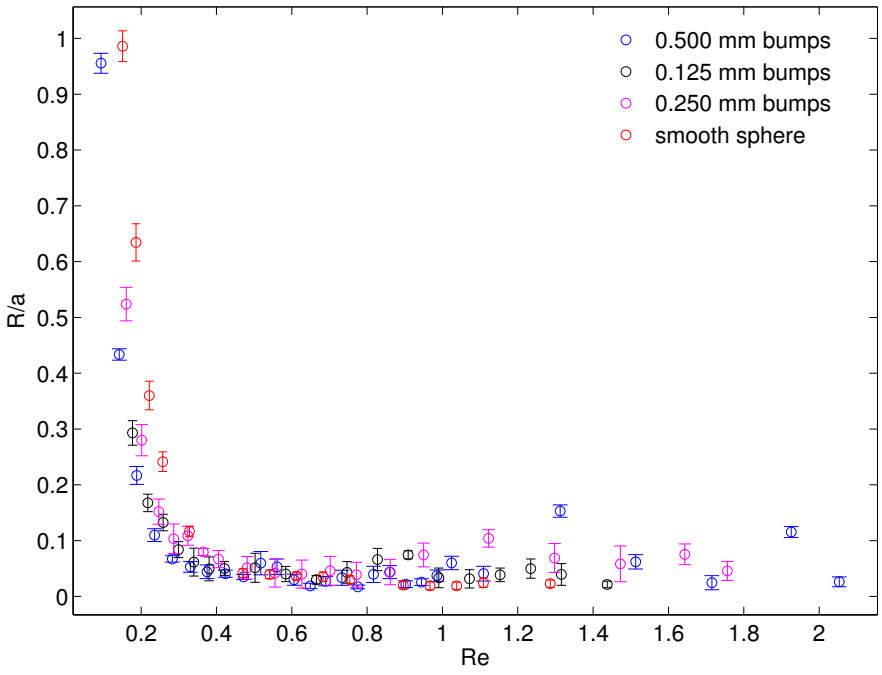

Figure 6.4: Orbital radius described by the rough spheres as a function of the Reynolds number. Magenta corresponds, to the orbital radius of a sphere with $a_{max} = 6.5$, black to $a_{max} = 7$ and blue to $a_{max} = 8$. The red circles correspond to the orbital radius of a smooth sphere of radius $a = 7$ mm.

Outer radius a_{max} [mm]	Re_c
6.5	0.38 ± 0.025
7	0.48 ± 0.035
8	0.35 ± 0.020
7 (smooth)	0.47 ± 0.04

Table 6.1: Critical Reynolds Re_c for the onset of oscillations, defined as the Re at which the measured orbital radius is greater than 5% the radius of the sphere.

In figure 6.4 the radius of the orbits of the spheres of different roughness is shown as a function of the Reynolds number. Here, it can be seen that the radius of the orbit obtained for the three different roughness studied here, does not differ in a significant manner over the range of roughness investigated. Moreover, the orbital radius of the rough spheres does not differ from the orbital radius of a smooth sphere with the same, in the case of the sphere with the biggest roughness, or similar, in the case of the other rough spheres, average radius.

The critical Reynolds number Re_c for the spheres of different roughness and the smooth sphere is shown in table 6.1. This is defined as the Re at which the measured orbital radius is greater than 5% the radius of the sphere.

It can be observed from this table that the onset of the oscillations occur at approximately the same Reynolds number for all the spheres, independent of their roughness. All the spheres start to oscillate at $Re_c = 0.42 \pm 0.06$.

6.3 Summary

The effect of surface roughness on the stability of the fixed point behaviour of a positively buoyant sphere inside a rotating cylinder was studied for three different roughness.

It was observed that the fixed point behaviour found previously for smooth spheres also exist for rough spheres. Moreover, when the average position of the three rough spheres is compared with the average position of a smooth sphere with the same average radius and density, the average position is the same, within experimental error, in all four cases. This result suggest that added roughness does not have a significant effect on the fixed point behaviour of a positively buoyant sphere.

Beyond the critical Reynolds number Re_c the fixed point became unstable and the rough sphere described circular orbits about the original fixed point, in a similar manner as the smooth sphere does. Furthermore, the orbital radius have the same functional dependance on the Reynolds number as that of a smooth sphere of equivalent average radius and equal density. The onset of the oscillations also occurs approximately at the same critical Reynolds number than for a smooth sphere.

Chapter 7

Conclusion

The investigation presented in this thesis concerned an experimental study on the dynamics of a positively buoyant sphere immersed in a rotating viscous flow. Careful experiments were conducted using different types of spheres inside of a horizontally rotating cylinder filled with glycerol. Different dynamical regimes were characterised, and the dependance of the dynamics of the sphere on the Reynolds number was studied for different sizes, roughness and for a hollow porous sphere that resembles a porous biological scaffold.

This study has shown that a sphere in this flow configuration has a rich family of dynamical behaviours. When increasing Re from zero, the sphere lays in a fixed point by the wall. This fixed point becomes unstable and he sphere starts oscillating vertically for $Re \approx 0.01$. When decreasing Re from $Re \approx 2$, the sphere lays at a fixed point at the axis of rotation of the flow, for $1 > Re > 0.2$ approximately, the sphere is at a eccentric fixed point and below that value of Re, the fixed point became unstable and the sphere started oscillating periodically, describing circular orbits about the original fixed point. A summary of the main findings and conclusions drawn for each

sphere type is provided in this chapter and some ideas for future research are outlined.

7.1 A Smooth Sphere

The average position of the centre of a smooth sphere, measured from the central axis of the cylinder, was obtained for spheres of different sizes. It has been observed that the smooth spheres have a range of eccentric fixed points. These fixed points become unstable below a critical Reynolds number Re_c. This instability corresponds to a simple periodic motion, the sphere describes a circular orbit centred at the original fixed point. Because the orbit is circular, the average position of the sphere when orbiting, corresponds to the orbital centre.

The theoretical model, developed by Johnson [44] and presented in chapter 3 prognosticated that the sphere should have a range of equilibrium positions. However, the stability analysis of these equilibrium positions is yet to be completed.

The agreement between the theoretical model of Johnson [44] and the position of the fixed points described in chapter 3 is very good. The model also predicts well the position of the centre of the orbits once the fixed point has become unstable and the sphere described circular orbits. This agreement between the discussed theory and the experimental data obtained in this thesis shed light on which are the relevant forces that describe this system: a viscous drag F_D, the centripetal force F_C and the buoyancy force F_B. These forces are enough to describe the eccentric equilibrium position and the centre of the oscillations after the sphere becomes unstable. The model

that was developed in the limit of very low Re works best for $Re < 0.5$ in this experiment, over this value some differences between the experimental positions and the theory can be observed.

It was also found that the stability range of the fixed points depends on the size of the sphere. Our results suggest that the stability range is proportional to the size of the sphere, meaning that a larger sphere has a larger stability range. The limit where the size of the sphere tends to zero is of particular interest, because the stability range of the eccentric fixed point would tend to zero as well, connecting the existent Stokesian calculations for a point like particle (that only has one equilibrium position at the central axis of the cylinder), with the theoretical calculations for finite radius and Re.

It would be interesting to do a similar study with an air bubble and compare them with the experimental results presented in this thesis. Some studies about the lift and the drag have already been made by Van Nieropp et al. [28] and Lohse et al. [29]. But a full characterisation of the dynamics of a bubble is still lacking.

It was shown that the orbital radius has an unusual growth rate that suggests the presence of a feedback mechanism in the orbits that grow from the fixed points. Considering that the sphere is free to move, this might be given by a resonance between the sphere and the wake which is left behind the sphere. Finally, it was shown that the circular orbits described in chapter 4 are not a result of resonances in the system, and that a periodic perturbation does not have a significant effect in the rotation of the sphere.

It is suggested that flow visualisation is used to observe what happens with the flow near the onset of the oscillation. This could provide an ex-

planation for the odd growth rate observed in this thesis, given that near the onset $Re > 0.5$ and some inertial effects could be observed. It would be particularly interesting to observe if there is a wake affecting the growth rate of the oscillations.

It has been observed that, when the Reynolds number is increased from zero up to $Re = 0.01$, the sphere stays at a fixed point by the wall of the cylinder. Over that value of Re, this fixed point became unstable and the sphere oscillated vertically. These near wall oscillations are described by a Hopf bifurcation because the motion is periodic and the amplitude grows as the square root of the Reynolds number. This coincides with the kind of bifurcation that was reported previously by Mullin [23] and Otto [53] for a heavy sphere oscillating near the wall of a rotating cylinder.

7.2 A Porous Sphere

The dynamics of a porous sphere immersed in a rotating viscous flow was studied experimentally and compared with the dynamics of a smooth solid sphere of similar size.

An eccentric equilibrium position exists for a porous sphere, but in comparison to the solid case, the fixed point is closer to the central axis of the cylinder and experimentally is much more difficult to detect. Nevertheless, the model [44] still predicts the equilibrium position of the porous sphere, if the terminal velocity to be considered in the model, is the one that has been measured experimentally. This is despite the fact that the model assumes that the sphere is solid. This is because the measurement of the terminal velocity contains information of the drag force acting on the sphere.

The porous sphere, as the solid on, describes circular orbits about a point off the central axis of the cylinder, and this point is still predicted by the model. In comparison with a solid sphere of similar size, the porous sphere has a bigger stability range, meaning it remains without oscillating for lower Reynolds numbers than the solid sphere.

The porous sphere, when increasing the Re form rest, lays at a fixed point by the wall. The behaviour of the porous sphere when oscillating by the wall is qualitatively similar to the onset of the oscillations for the solid sphere. The onset of the oscillations also occurred to a similar Reynolds number $Re = 0.01$.

Regarding the dynamics of a biological scaffold, these results suggest that the porosity can have a stabilising effect, increasing the Reynolds number range at which tissue can be grown inside of a rotating bioreactor, avoiding the onset of oscillations. It is also important to notice that porosity decreases the shear stress acting on the scaffold, which could have an effect on the tissue metabolism due to the unknown biological response of the tissue to shear stress.

7.3 Rough Spheres

The effect of the surface roughness on the stability of the fixed point behaviour of a positively buoyant sphere inside a rotating viscous flow was studied for three different roughness. It was observed that the fixed point behaviour found previously for smooth spheres also exist for rough spheres. Moreover, when the average position of the three rough spheres is compared with the average position of a smooth sphere with the same average radius

and density, it can be seen that the average position is the same in all four cases. This result suggests that added roughness does not have an effect on the fixed point behaviour of a light sphere.

It was also observed that when the fixed point became unstable, the rough sphere described circular orbits, as the smooth sphere did. Furthermore, the orbits had the same functional dependance on the Reynolds number as that of a smooth sphere of equivalent average radius.

The fact that the behaviour of the rough spheres does not seem to have an effect on the fixed points or the orbits, when compared with a smooth sphere of equivalent average radius, is a relevant result, it means the fixed points and orbits are robust to this kind of perturbations on the shape of the sphere.

It would be interesting to investigate the effect that shape could have on the eccentric fixed points observed in this thesis. Given that in the case of a heavy sphere compared to a heavy ellipsoid, quantitative and qualitative differences were found when comparing their behaviours near the wall.

Bibliography

[1] Sir William Thomson. On the ultramundane corpuscles of le sage, also on the motion of rigid solids in a liquid circulating irrationally through perforations in them or in a filled solid. *The London, Edinburgh and Dublin Philosophical Magazine and Journal of Science*, 45:321–245, 1873.

[2] Ray P Schwarz and David A Wolf. Rotating bio-reactor cell culture apparatus. *US-PATENT-4.988.623, US-PATENT-APPL-SN-213559, NASA-CASE-MSC-21293-1*, 1991.

[3] Elisabeth Guazzelli and Jeffrey F Morris. *A physical introduction to suspension dynamics*, volume 45. Cambridge University Press, 2011.

[4] Glyn O. Roberts, Dale M. Kornfeld, and William W. Fowlis. Particle orbits in a rotating liquid. *Journal of Fluid Mechanics*, 229:555–567, 8 1991.

[5] JH Kim, ED Sudol, MS El-Aasser, JW Vanderhoff, and DM Kornfeld. Preparation of large-particle-size monodisperse latexes in a rotating-cylinder reactor. *Chemical engineering science*, 43(8):2025–2030, 1988.

[6] TJ Pedley and JO Kessler. Bioconvection. *Science Progress (1933-)*, pages 105–123, 1992.

[7] NA Hill and TJ Pedley. Bioconvection. *Fluid Dynamics Research*, 37(1):1–20, 2005.

[8] Department of Health and Human Services USA.gov National Institutes of Health. https://www.nibib.nih.gov/science-education/science-topics/tissue-engineering-and-regenerative-medicine.

[9] NASA Official: Dan Lockney. https://spinoff.nasa.gov/Spinoff2011/hm_1.html.

[10] David A Wolf and Ray P Schwarz. Analysis of gravity-induced particle motion and fluid perfusion flow in the nasa-designed rotating zero-headspace tissue culture vessel. *NASA Technical Paper*, 1991.

[11] Mohit Dalwadi. *Flow and nutrient transport problems in rotating bioreactor systems*. PhD thesis, University of Oxford, Lincoln College, 2014.

[12] Brian R Unsworth and Peter I Lelkes. Growing tissues in microgravity. *Nature medicine*, 4(8):901–907, 1998.

[13] H Gao, PS Ayyaswamy, and P Ducheyne. Dynamics of a microcarrier particle in the simulated microgravity environment of a rotating-wall vessel. *Microgravity science and technology*, 10(3):154–165, 1996.

[14] Vassilios I Sikavitsas, Gregory N Bancroft, and Antonios G Mikos. Formation of three-dimensional cell/polymer constructs for bone tissue engineering in a spinner flask and a rotating wall vessel bioreactor. *Journal of biomedical materials research*, 62(1):136–148, 2002.

[15] Aaron S Goldstein, Tiffany M Juarez, Christopher D Helmke, Michael C Gustin, and Antonios G Mikos. Effect of convection on osteoblastic cell

growth and function in biodegradable polymer foam scaffolds. *Biomaterials*, 22(11):1279–1288, 2001.

[16] Robert S Cherry and Eleftherios Terry Papoutsakis. Physical mechanisms of cell damage in microcarrier cell culture bioreactors. *Biotechnology and bioengineering*, 32(8):1001–1014, 1988.

[17] RD ODea, HM Byrne, and SL Waters. Continuum modelling of in vitro tissue engineering: a review. In *Computational Modeling in Tissue Engineering*, pages 229–266. Springer, 2012.

[18] Xiaojun Yu, Edward A Botchwey, Elliot M Levine, Solomon R Pollack, and Cato T Laurencin. Bioreactor-based bone tissue engineering: the influence of dynamic flow on osteoblast phenotypic expression and matrix mineralization. *Proceedings of the National Academy of Sciences of the United States of America*, 101(31):11203–11208, 2004.

[19] SR Pollack, DF Meaney, EM Levine, M Litt, and ED Johnston. Numerical model and experimental validation of microcarrier motion in a rotating bioreactor. *Tissue engineering*, 6(5):519–530, 2000.

[20] Scott J Hollister. Porous scaffold design for tissue engineering. *Nature materials*, 4(7):518–524, 2005.

[21] Elsie S Place, Nicholas D Evans, and Molly M Stevens. Complexity in biomaterials for tissue engineering. *Nature materials*, 8(6):457–470, 2009.

[22] Marcello Lappa. Organic tissues in rotating bioreactors: Fluid-

mechanical aspects, dynamic growth models, and morphological evolution. *Biotechnology and bioengineering*, 84(5):518–532, 2003.

[23] T Mullin, Y Li, C Del Pino, and J Ashmore. An experimental study of fixed points and chaos in the motion of spheres in a stokes flow. *IMA journal of applied mathematics*, 70(5):666–676, 2005.

[24] J Ashmore, C Del Pino, and T Mullin. Cavitation in a lubrication flow between a moving sphere and a boundary. *Physical review letters*, 94(12):124501, 2005.

[25] Yoshiyuki Tagawa, Jarich van der Molen, Leen van Wijngaarden, and Chao Sun. Wall forces on a sphere in a rotating liquid-filled cylinder. *Physics of Fluids (1994-present)*, 25(6):063302, 2013.

[26] L Yang, JRT Seddon, T Mullin, C Del Pino, and J Ashmore. The motion of a rough particle in a stokes flow adjacent to a boundary. *Journal of Fluid Mechanics*, 557:337–346, 2006.

[27] Paul F Tooby, Gerald L Wick, and John D Isaacs. The motion of a small sphere in a rotating velocity field: a possible mechanism for suspending particles in turbulence. *Journal of Geophysical Research*, 82(15):2096–2100, 1977.

[28] Ernst A Van Nierop, Stefan Luther, Johanna J Bluemink, Jacques Magnaudet, Andrea Prosperetti, and Detlef Lohse. Drag and lift forces on bubbles in a rotating flow. *Journal of Fluid Mechanics*, 571:439–454, 2007.

[29] Detlef Lohse and Andrea Prosperetti. Controlling bubbles. *Journal of Physics: Condensed Matter*, 15(1):S415, 2002.

[30] JJ Bluemink, D Lohse, A Prosperetti, and L Van Wijngaarden. Drag and lift forces on particles in a rotating flow. *Journal of fluid mechanics*, 643:1–31, 2010.

[31] JJ Bluemink, D Lohse, A Prosperetti, and L Van Wijngaarden. A sphere in a uniformly rotating or shearing flow. *Journal of Fluid Mechanics*, 600:201–233, 2008.

[32] Chao Sun, Tom Mullin, Leen Van Wijngaarden, and Detlef Lohse. Drag and lift forces on a counter-rotating cylinder in rotating flow. *Journal of fluid mechanics*, 664:150–173, 2010.

[33] James RT Seddon and Tom Mullin. Reverse rotation of a cylinder near a wall. *Physics of Fluids (1994-present)*, 18(4):041703, 2006.

[34] JRT Seddon and T Mullin. The motion of a prolate ellipsoid in a rotating stokes flow. *Journal of Fluid Mechanics*, 583:123–132, 2007.

[35] LD Landau and JB Sykes. Fluid mechanics: Vol 6. 1987.

[36] Lee and Anthony J. C. Ladd. Particle dynamics and pattern formation in a rotating suspension. *J. Fluid Mech.*, 577:183–209, 2005.

[37] JJM Magnaudet. The forces acting on bubbles and rigid particles. In *ASME Fluids Engineering Division Summer Meeting, FEDSM*, volume 97, pages 22–26, 1997.

[38] Alfred Barnard Basset. On the motion of a sphere in a viscous liquid. *Philosophical Transactions of the Royal Society of London. A*, 179:43–63, 1888.

[39] Joseph Boussinesq. Application des potentiels a l'ètude de l'équilibre et du mouvement des solides élastiques: mémoire suivi de notes étendues sur divers points de physique mathématique et d'analyse/par j. boussinesq. 1885.

[40] P. G. Saffman. The lift on a small sphere in a slow shear flow. *J. Fluid Mech.*, 22:385–400, 1965.

[41] P. G. Saffman. The lift on a small sphere in a slow shear flow. *J. Fluid Mech.*, 31:624, 1968.

[42] John B. McLaughlin. Inertial migration of a small sphere in linear shear flows. *Journal of Fluid Mechanics*, 224:261–274, 3 1991.

[43] Toshiyuki Gotoh. Brownian motion in a rotating flow. *Journal of Statistical Physics*, 59(1-2):371–402, 1990.

[44] Chris Johnson. private communication, 2015.

[45] Karthik Mukundakrishnan, Howard H Hu, and Portonovo S Ayyaswamy. The dynamics of two spherical particles in a confined rotating flow: pedalling motion. *Journal of Fluid Mechanics*, 599:169–204, 2008.

[46] LES Ramirez, EA Lim, CFM Coimbra, and MH Kobayashi. On the dynamics of a spherical scaffold in rotating bioreactors. *Biotechnology and bioengineering*, 84(3):382–389, 2003.

[47] Horace Lamb. *Hydrodynamics*. Cambridge university press, 1932.

[48] Vo Fidleris and RL Whitmore. Experimental determination of the wall effect for spheres falling axially in cylindrical vessels. *British journal of applied physics*, 12(9):490, 1961.

[49] Alfred W Francis. Wall effect in falling ball method for viscosity. *Journal of Applied Physics*, 4(11):403–406, 1933.

[50] Martin R Maxey and James J Riley. Equation of motion for a small rigid sphere in a nonuniform flow. *Physics of Fluids (1958-1988)*, 26(4):883–889, 1983.

[51] HP Greenspan and LN Howard. On a time-dependent motion of a rotating fluid. *Journal of fluid mechanics*, 17(03):385–404, 1963.

[52] Steven H Strogatz. *Nonlinear dynamics and chaos: with applications to physics, biology, chemistry, and engineering*. Westview press, 2014.

[53] Caren Otto. *The Motion of a Sphere in a Stokes Flow Near a Wall*. PhD thesis, The University of Manchester, 2009.